Bioorganic Chemistry 167 (2025) 109252

Contents lists available at ScienceDirect

Bioorganic Chemistry

journal homepage: www.elsevier.com/locate/bioorg

Dual targeting of neuroblastoma and cholinesterase by morpholino/pyrrolidino-sulfonyl-indole thiosemicarbazones: Synthesis, characterization, enzyme inhibition, cytotoxicity, docking and dynamics studies

Zahra Batool [a], Gülbahar Özge Alim Toraman [b], Furkan Çakır [c], Gülaçtı Topçu [b], Parham Taslimi [d], Rima D. Alharthy [e], Ajmal Khan [f,g,*], Ahmed Al-Harrasi [f], Zahid Shafiq [a,**], Halil Şenol [c,***]

[a] Institute of Chemical Sciences, Bahauddin Zakariya University, 60800 Multan, Pakistan
[b] Department of Pharmacognosy, Faculty of Pharmacy, Bezmialem Vakif University, 34093 Fatih, Istanbul, Türkiye
[c] Department of Pharmaceutical Chemistry, Faculty of Pharmacy, Bezmialem Vakif University, 34093 Fatih, Istanbul, Türkiye
[d] Department of Biotechnology, Faculty of Science, Bartin University, 74110 Bartin, Türkiye
[e] Department of Chemistry, Science & Arts College, Rabigh Branch, King Abdulaziz University, Rabigh 21911, Saudi Arabia
[f] Natural and Medical Sciences Research Centre, University of Nizwa, P.O. Box 33, PC 616, Birkat Al Mauz, Nizwa, Sultanate of Oman
[g] Department of Chemical and Biological Engineering, College of Engineering, Korea University, 145 Anam-ro, Seongbuk-gu, Seoul 02841, Republic of Korea

ARTICLE INFO

Keywords:
Morpholinosulfonyl
Pyrrolosulfonyl
Neuroblastoma
Cholinesterase
Cytotoxicity
Molecular docking
Molecular dynamics
Enzyme kinetics

ABSTRACT

In this study, twenty novel morpholino/pyrrolidino-sulfonyl-indole thiosemicarbazone derivatives (**6a-j** and **7a-j**) were synthesized and tested for cholinesterase inhibition and anticancer activity. Compounds **6h** and **7h** stood out as the most potent inhibitors of acetylcholinesterase (AChE) and butyrylcholinesterase (BChE), with IC_{50} values as low as 0.15 μM and 0.12 μM, respectively, outperforming reference drugs tacrine and galantamine. Both also showed significant cytotoxicity against SH-SY5Y neuroblastoma cells, with IC_{50} values of 3.8 μM and 4.2 μM, and high selectivity indices (126 for **6h** and 60 for **7h**) compared to normal fibroblast cells, indicating therapeutic potential. Molecular docking and MM-GBSA analyses revealed strong binding affinities with docking scores between −8.7 and − 9.3 kcal/mol and ΔG bind ranging from −55 to −62 kcal/mol. Key residues such as Trp-86, Tyr-341, Tyr-337, and Tyr-124 in AChE and Trp-82, Phe-329, Trp-231, and Pro-329 in BChE facilitated stable hydrogen bonds and π–π stacking. Molecular dynamics simulations over 250 ns confirmed complex stability with low RMSD and RMSF values. These combined results highlight **6h** and **7h** as promising multitarget therapeutic candidates for neurodegenerative diseases and cancer.

1. Introduction

Cancer is a complex group of diseases characterized by uncontrolled cell proliferation and the potential to invade or spread to other parts of the body. It remains a major global health problem, ranking as the second leading cause of death worldwide. According to the Global Cancer Observatory 2024 estimates, over 20 million new cancer cases and approximately 10 million cancer-related deaths were recorded globally. These numbers are projected to rise significantly in the coming decades due to aging populations, lifestyle changes, and environmental factors [1–3].

Neuroblastoma is the most common extracranial solid tumor in children, primarily affecting those under five. Arising from sympathetic nervous system tissues, it accounts for 7–10 % of childhood cancers and

* Corresponding author.
** Corresponding author.
*** Corresponding author.
E-mail addresses: zahra.bhatti6469@gmail.com (Z. Batool), galim@bezmialem.edu.tr (G.Ö.A. Toraman), furkan.cakir@bezmialem.edu.tr (F. Çakır), gtopcu@bezmialem.edu.tr (G. Topçu), ptaslimi@bartin.edu.tr (P. Taslimi), iaaalharte@kau.edu.sa (R.D. Alharthy), ajmalkhan@unizwa.edu.om (A. Khan), aharrasi@unizwa.edu.om (A. Al-Harrasi), zahidshafiq@bzu.edu.pk (Z. Shafiq), hsenol@bezmialem.edu.tr (H. Şenol).

https://doi.org/10.1016/j.bioorg.2025.109252
Received 26 August 2025; Received in revised form 25 October 2025; Accepted 12 November 2025
Available online 14 November 2025

around 15 % of pediatric cancer deaths [4]. Its clinical course varies widely, from spontaneous regression to aggressive, metastatic disease [5]. High-risk cases, typically diagnosed at advanced stages, remain challenging to treat and are associated with poor outcomes despite intensive multimodal therapies [6–10]. Various pathways, including TMEM64-mediated activation, m6A-driven upregulation of lncRNA CHASERR, and LINC00346-associated inflammatory signaling, have been reported to promote glioma proliferation, migration, and immune infiltration.[11–13].

Cholinesterases, including acetylcholinesterase (AChE) and butyrylcholinesterase (BChE), are key enzymes responsible for the hydrolysis of the neurotransmitter acetylcholine in the synaptic cleft, thereby regulating cholinergic neurotransmission [14–17]. Inhibition of these enzymes has significant pharmacological relevance, particularly in the treatment of neurodegenerative diseases such as Alzheimer's disease. By inhibiting cholinesterases, the levels of acetylcholine are increased in the synapse, leading to improved cognitive function in patients with cholinergic deficits [18].

Beyond neurodegenerative conditions, cholinesterase inhibitors have been explored for their roles in managing myasthenia gravis, glaucoma, and certain types of poisoning (e.g., organophosphates). Moreover, recent studies suggest that cholinesterase activity is also linked to tumor progression and immune regulation, making these enzymes potential targets in cancer therapy as well. Therefore, the development of novel cholinesterase inhibitors not only contributes to neurological disorder treatment but also offers a broader therapeutic potential in oncology and inflammation [19–25].

Although neuroblastoma and Alzheimer's disease differ in age of onset and clinical features, they share key molecular mechanisms. Both involve the cholinergic system, particularly through acetylcholinesterase (AChE) and butyrylcholinesterase (BChE) activity. While cholinesterase inhibitors are used in Alzheimer's to boost acetylcholine levels, neuroblastoma cells also express these enzymes, suggesting a role in tumor behavior. Additionally, shared factors such as amyloid precursor protein (APP), NGF, and BDNF, and inhibition of phosphorylation of IκBα and p38 contribute to cell survival and differentiation in both diseases. These overlaps highlight potential cross-disease therapeutic strategies targeting neural pathways [26–29].

Thiosemicarbazones are bioactive compounds with diverse effects, including anticancer, antimicrobial, and enzyme inhibition [30–32]. Their metal-chelating ability disrupts key enzymes and promotes apoptosis, making them promising candidates for drug development across multiple diseases [30,33–39]. Morpholine, pyrroline, sulfonamide, and indole are well-known pharmacophores with complementary properties [40–46]. Morpholine enhances solubility and pharmacokinetics, sulfonamides offer antibacterial and enzyme-inhibitory effects, and indole enables strong target interactions. Combining different pharmacophores into a single hybrid molecule may yield synergistic effects, improving selectivity and therapeutic potential [47], especially for cancer and neurodegenerative disorders [48–57].

Hydrazone derivatives, which share the characteristic C═N (imine) linkage with thiosemicarbazones, have also attracted considerable interest due to their diverse biological activities. This structural similarity often imparts comparable metal-chelating and enzyme-inhibitory properties, supporting the pharmacological relevance of thiosemicarbazone scaffolds [58–62].

The rational design of hybrid compounds combining morpholine, sulfonamide, and indole is based on their complementary bioactivities [63,64]. Indole offers strong target interactions, sulfonamides provide enzyme inhibition and anti-inflammatory effects, and morpholine improves solubility and pharmacokinetics. Merging these moieties aims to enhance multitarget potential, selectivity, and bioavailability, offering a promising approach for treating complex diseases like cancer and Alzheimer's. [65,66]. (Scheme 1).

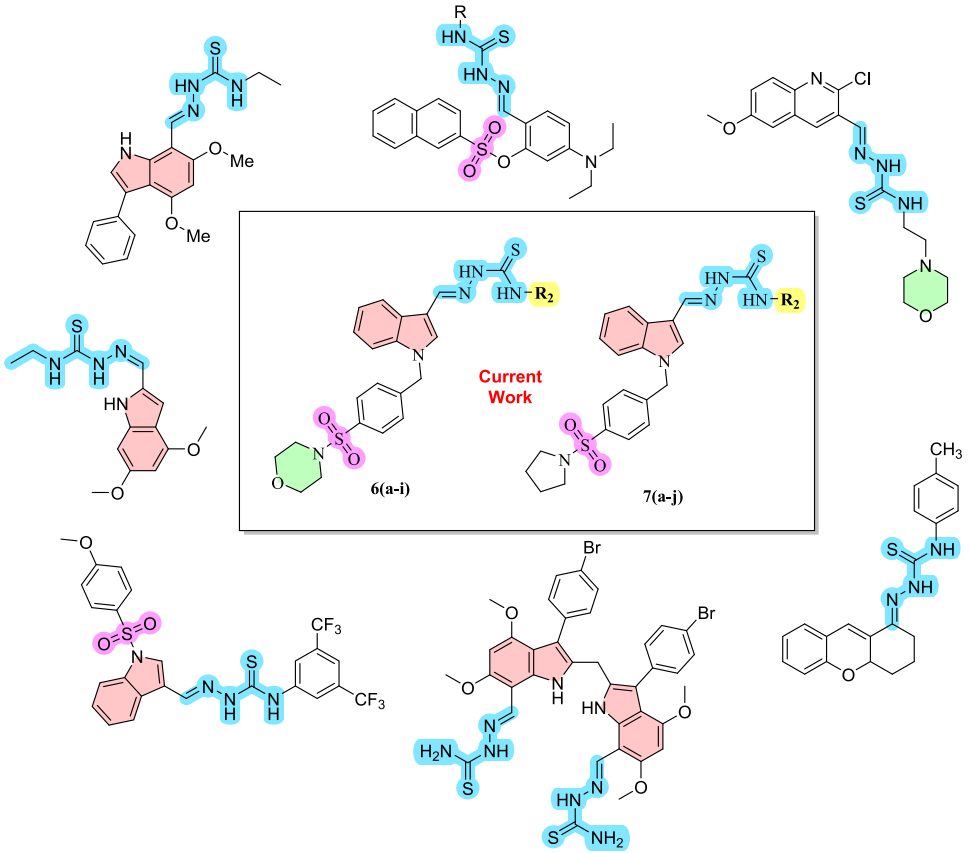

Scheme 1. Some AChE/BChE active thiosemicarbazones and the target compounds of the current study

This study aimed to synthesize and characterize 20 novel morpholino/pyrrolidino-sulfonyl-indole thiosemicarbazone derivatives and evaluate their biological activities, focusing on neuroblastoma and cholinesterase enzymes. Their cytotoxicity was tested on SH-SY5Y neuroblastoma and healthy CCD-1079Sk cells. Inhibitory effects on acetylcholinesterase (AChE) and butyrylcholinesterase (BChE) were assessed with enzyme kinetics. Molecular docking, dynamics simulations, and ADMET predictions were used to analyze binding, stability, and pharmacokinetics. This approach seeks to identify multitarget agents for neuroblastoma and cholinesterase-related disorders.

2. Results and discussion

2.1. Chemistry

In this study, 20 novel morpholino/pyrrolidino-sulfonyl-indole thiosemicarbazone derivatives were synthesized, and their characterization was performed using NMR, HRMS, and IR techniques (Scheme 2).

The formation of N-substituted indole-based thiosemicarbazones **6 (a-j)** and **7(a-j)** was confirmed by their ^{1}H & ^{13}C NMR. The presence of two singlets for NH protons at 12.01–11.21 ppm and 10.11–8.34 ppm and a singlet at 8.48–8.02 ppm for the azomethine proton in the 1-H NMR spectrum of representative thiosemicarbazone **6(a-j)** and **7(a-j)** suggests the successful condensation of thiosemicarbazide at the aldehydic position of indole. In the 13C NMR, peaks at 185.31–174.29 and 174.28–143.05 ppm can be attributed to the presence of C═S and C═N, respectively.

In the fluorinated derivatives (**6h** and **7h**), the F—C spin–spin coupling analyses are presented in detail in Fig. 1. As compounds **6h** and **7h** are also the most potent molecules in this study, a more advanced structural characterization of these compounds is particularly important. The only difference between compounds **6h** and **7h** arises from the substituent at the terminal sulfonyl group: a morpholine ring in **6 h** and a pyrrolidine ring in **7h**. Therefore, the F—C spin–spin couplings within the fluorophenyl ring are nearly identical in both compounds.

In both **6h** and **7h**, the carbon directly bonded to fluorine (C24 position) exhibits a spin–spin splitting in the ^{13}C NMR spectrum as a doublet at 160.03 ppm, with corresponding signals at 160.83 and 159.22 ppm, and a coupling constant $J = 241.7$ Hz. In compound **6h**, the ortho carbon to fluorine (C23) appears as a doublet at 115.19 ppm with a J value of 22.7 Hz, whereas in compound **7h** this value is 22.5 Hz. The meta carbon positions (C22) in both compounds show doublet splitting with a J value of 9.1 Hz; however, in both cases, one of the doublet signals overlaps with other aromatic carbon signals. Finally, the para carbon (C21) resonates as a doublet at 136.17 ppm with a J value of 2.9 Hz in both compounds.

2.2. Enzyme inhibition

To evaluate cholinesterase inhibitory activity, the synthesized compounds were tested against AChE and BChE using standard in vitro assays. Both enzymes play crucial roles in cholinergic neurotransmission and are key targets in the treatment of neurodegenerative diseases. The inhibitory effects were expressed as IC_{50} values to assess potency and selectivity. Additionally, kinetic studies were conducted for the most active compounds to determine their inhibition constants (K_i), offering further insight into enzyme-inhibitor interactions. The cholinesterase inhibitory activities of the synthesized thiosemicarbazone derivatives were systematically evaluated against AChE and BChE, with the corresponding IC_{50} and K_i values presented in Table 1.

Most compounds exhibited strong inhibitory effects against AChE, with IC_{50} values in the low nanomolar range. For example, compound **6h** showed an exceptionally low IC_{50} of 0.13 nM, indicating extremely high potency. This is significantly better than the reference drug tacrine (5.82 nM) and galantamine (17.06 nM), commonly used AChE inhibitors. Similarly, compound **7h** demonstrated remarkable inhibition with an IC_{50} of 0.10 nM. The K_i values, which reflect the binding affinity of the inhibitors to the enzyme, paralleled the IC_{50} results, further confirming that these compounds tightly bind to the enzyme active site. For instance, **6h**'s K_i of 0.09 nM shows powerful competitive binding to AChE, which suggests efficient displacement of the natural substrate (Fig. 2).

While AChE inhibition was generally stronger, several compounds also showed moderate to good activity against BChE, with IC_{50} values ranging from approximately 9 to 47 nM. Compound **6h** had one of the best BChE inhibition values (11.3 nM), and **7h** also showed good dual inhibition (17.27 nM).

Compounds **6c, 6e,** and **6j,** for example, exhibit low nanomolar IC_{50} values against AChE (ranging from about 0.6 to 0.7 nM), which are significantly better than tacrine and galantamine. Their corresponding K_i values confirm strong binding affinity, indicating that these compounds are effective competitive inhibitors. In contrast, compounds

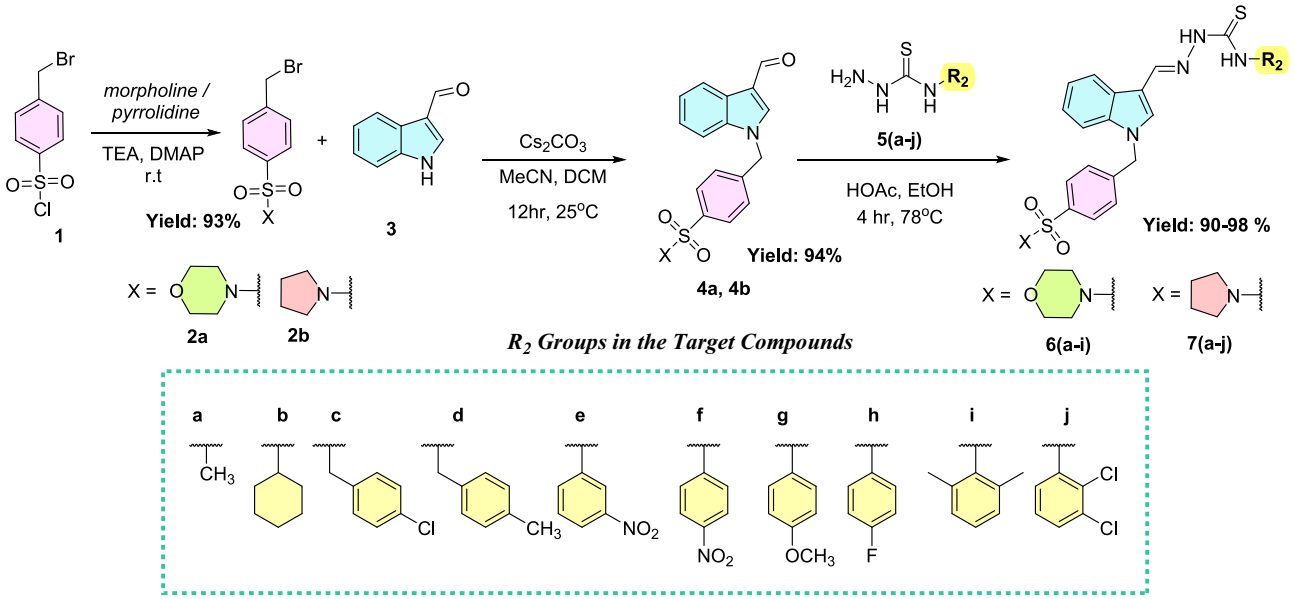

Scheme 2. Synthetic pathways of the target compounds

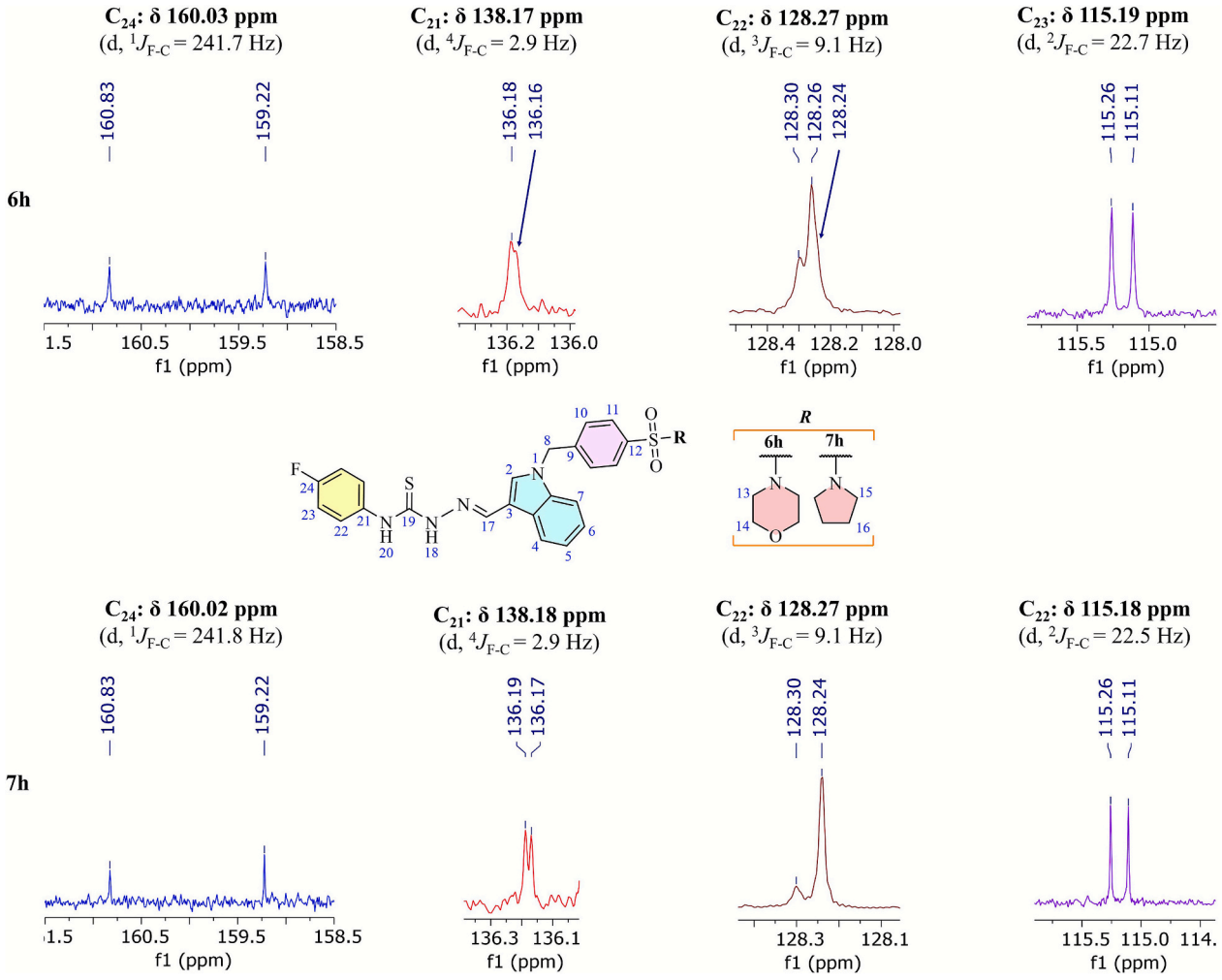

Fig. 1. The ^{13}C NMR F—C coupling analysis of compounds **6h** and **7h.**

such as **6b, 6d,** and **6i** show higher IC_{50} values against both AChE and BChE, suggesting comparatively weaker inhibition. For instance, **6b**'s IC_{50} for AChE is 8.33 nM, which is still potent but less so than the more active analogues. Regarding BChE inhibition, compounds like **6f** and **7c** show promising activity with IC_{50} values around 11–12 nM. While these values are higher than their AChE inhibition, they indicate a degree of dual inhibition that could be therapeutically beneficial, as BChE activity increases in late-stage Alzheimer's disease.

As a results, the data show that small changes in the chemical structure of these hydrazone derivatives greatly affect their strength and selectivity as enzyme inhibitors. All compounds act as competitive inhibitors. Among the tested compounds, **6h** and **7h** stand out as the most potent inhibitors, showing stronger activity than standard drugs like tacrine and galantamine.

2.3. Cytotoxic activity

The cytotoxicity assays were performed using the human neuroblastoma cell line SH-SY5Y to evaluate anticancer potential, while the healthy human skin fibroblast cell line CCD-1079Sk was used to assess the selectivity and safety profile of the compounds. The half-maximal inhibitory concentration (IC_{50}) values are summarized in Table 2.

The cytotoxic activities of the synthesized thiosemicarbazone derivatives **(6a–6j** and **7b–7j)** were evaluated against SH-SY5Y neuroblastoma and CCD-1079Sk healthy human fibroblast cell lines. The results, presented as IC_{50} values in μM, revealed a wide range of cytotoxic potentials among the derivatives. Notably, compound **6a** exhibited the strongest antiproliferative effect on SH-SY5Y cells with an IC_{50} of 0.51 μM, while demonstrating minimal toxicity to healthy cells (IC_{50} = 64.52 μM), resulting in an exceptionally high selectivity index (SI) of 126.5. Similarly, compounds **7h** and **7j** also showed remarkable potency (IC_{50} = 0.87 and 0.91 μM, respectively) along with high selectivity (SI = 60.1 and 49.6, respectively), positioning them as the most promising candidates in the series.

Other derivatives such as **6f** (IC_{50} = 0.92 μM, SI = 31.8), **6j** (0.66 μM, SI = 26.0), and **7f** (1.54 μM, SI = 23.0) also demonstrated strong cytotoxic effects against SH-SY5Y cells while maintaining good selectivity over healthy cells, which supports their potential for further development. On the other hand, derivatives like **6a** and **7c**, with SI values below 5, showed poor selectivity, suggesting non-specific toxicity that may limit their therapeutic applications.

When compared to the reference compound sorafenib, which exhibited an IC_{50} of 3.82 μM on SH-SY5Y and an SI of only 4.7, many of the synthesized derivatives, particularly **6h, 7h,** and **7j**, offered superior cytotoxic potency and selectivity profiles. This contrast underscores the enhanced therapeutic potential of these new molecules. Additionally, several compounds such as **6b, 6e, 6g, 6i, 7b, 7g,** and **7i** displayed IC_{50} values in the 1–3 μM range and moderate SI values between 10 and 20, suggesting a balance between efficacy and safety.

Taken together, these findings indicate that many of the synthesized compounds are not only effective in inhibiting neuroblastoma cell proliferation but also possess favorable safety margins, especially in comparison with existing reference drugs. Compounds **6h** and **7h,** with their low IC_{50} values and high SI, emerge as leading candidates for further

Table 1
IC_{50} and K_i values of title compounds against AChE and BChE.

		IC_{50} (nM)		K_i (nM)	
Title	**R_2 group**	**AChE**	**BChE**	**AChE**	**BChE**
6a	Methyl	2.81 ± 0.05	28.85 ± 1.24	1.50 ± 0.05	23.34 ± 2.97
6b	Cyclohexyl	8.33 ± 0.08	32.84 ± 2.58	5.91 ± 0.16	26.60 ± 1.83
6c	4-chloro-benzyl	0.61 ± 0.02	16.92 ± 1.57	0.53 ± 0.08	12.32 ± 1.90
6d	4-methylbenzyl	7.14 ± 0.05	46.52 ± 3.61	5.68 ± 0.24	34.54 ± 2.35
6e	3-nitrophenyl	0.62 ± 0.03	17.70 ± 2.01	0.44 ± 0.08	13.83 ± 1.01
6f	4-nitrophenyl	0.46 ± 0.01	11.30 ± 0.60	0.26 ± 0.03	8.67 ± 0.89
6g	4-methoxyphenyl	6.13 ± 0.09	27.60 ± 3.27	4.50 ± 0.11	23.34 ± 1.54
6h	**4-fluorophenyl**	**0.13 ± 0.02**	**12.34 ± 0.84**	**0.09 ± 0.01**	**9.95 ± 0.62**
6i	2,6-dimethylphenyl	7.67 ± 0.08	31.33 ± 1.52	5.13 ± 0.55	27.66 ± 2.05
6j	2,3-dichlorophenyl	0.71 ± 0.03	16.53 ± 1.33	0.40 ± 0.05	11.17 ± 0.94
7a	Methyl	4.14 ± 0.04	21.80 ± 2.27	3.67 ± 0.14	16.72 ± 1.68
7b	Cyclohexyl	3.50 ± 0.05	31.40 ± 2.54	2.52 ± 0.06	24.70 ± 3.62
7c	3-chlorobenzyl	1.57 ± 0.03	11.27 ± 0.60	1.24 ± 0.03	9.30 ± 0.73
7d	4-methylbenzyl	4.72 ± 0.06	29.62 ± 3.72	2.98 ± 0.25	21.63 ± 2.57
7e	3-nitrophenyl	0.98 ± 0.01	13.58 ± 1.02	0.70 ± 0.02	10.78 ± 0.70
7f	4-nitrophenyl	1.56 ± 0.04	14.71 ± 1.36	1.15 ± 0.02	11.76 ± 0.75
7g	4-methoxyphenyl	3.71 ± 0.04	29.32 ± 3.03	2.56 ± 0.27	21.76 ± 1.60
7h	**4-fluorophenyl**	**0.10 ± 0.01**	**17.27 ± 1.74**	**0.08 ± 0.01**	**7.27 ± 0.84**
7i	2,6-dimethylphenyl	4.18 ± 0.06	26.16 ± 1.75	3.54 ± 0.06	23.62 ± 1.56
7j	2,3-dichlorophenyl	0.34 ± 0.02	9.55 ± 0.92	0.24 ± 0.04	14.10 ± 0.97
Gal*		17.06 ± 2.15	43.12 ± 5.71	14.25 ± 1.67	38.05 ± 5.16
Tac*		5.82 ± 0.07	30.71 ± 2.46	4.60 ± 0.52	25.75 ± 2.57

* Tacrine and galantamine were used as reference drugs.

preclinical evaluation.

2.4. Structure-activity relationship (SAR)

Structure-activity relationship (SAR) analysis of the thiosemicarbazone derivatives revealed significant variations in biological activity depending on the R_2 substituent. Notably, compounds **6h** and **7h**, both bearing a 4-fluorophenyl group, exhibited the most potent inhibition of acetylcholinesterase (AChE) with remarkably low IC_{50} and K_i values. These compounds also showed high cytotoxicity against SH-SY5Y neuroblastoma cells while maintaining excellent selectivity toward healthy CCD-1079Sk fibroblasts, as reflected by their high selectivity indices. This suggests that the 4-fluorophenyl substituent enhances strong binding affinity to the enzyme active site and confers selective toxicity toward cancer cells (Scheme 3).

Similarly, halogenated derivatives such as **6j** (2,3-dichlorophenyl) and **7j** (2,3-dichlorophenyl) demonstrated strong AChE inhibition, though their potency and selectivity were slightly lower than those of the fluorinated compounds. Nitro-substituted compounds like **6f** and **7f** showed moderate inhibitory activity and cytotoxicity, whereas derivatives with alkyl groups such as methyl or cyclohexyl (e.g., **6a, 7a,** and **7b**) exhibited comparatively weaker enzyme inhibition and lower selectivity.

Overall, the SAR findings highlight that the 4-fluorophenyl-containing compounds **6h** and **7h** are the most promising candidates in this series, combining potent AChE inhibition with favorable selectivity profiles.

2.5. Molecular docking studies

To further explore the molecular basis of enzyme inhibition, molecular docking and MM-GBSA (Molecular Mechanics Generalized Born Surface Area) calculations were conducted against AChE, BChE, and the YAP-TEAD1 proteins. In addition to cholinesterase inhibition, the most active compounds **(6h** and **7h)** were evaluated for their potential to disrupt the oncogenic YAP–TEAD1 complex, a key regulator in the Hippo pathway. In neuroblastoma, YAP (Yes-associated protein) and TEAD1 (TEA domain transcription factor 1) drive tumor growth and resistance. Docking studies showed that **6h** and **7h** could bind to the TEAD1 surface at the YAP-binding site, indicating their potential as dual-action agents targeting both cholinesterase activity and YAP–TEAD1-driven oncogenesis. For comparison, tacrine, galantamine, and sorafenib were included as reference compounds in the docking studies, and the results are summarized in Table 3.

Table 3 demonstrates that compounds **6h** and **7h** exhibit significantly stronger binding affinities toward AChE, BChE, and the YAP–TEAD1 complex compared to reference drugs. For AChE, compound **6c** showed the most favorable docking score (−12.50 kcal/mol) and binding free energy (−83.06 kcal/mol), outperforming both tacrine and galantamine. Similarly, compound **7h** also showed strong AChE binding (−11.38 / −69.65 kcal/mol). Against BChE, both compounds again demonstrated superior binding (−11.73 and − 11.21 kcal/mol; −71.32 and − 76.38 kcal/mol, respectively) relative to the reference inhibitors.

Notably, in the YAP–TEAD1 system, both **6h** and **7h** bound more strongly (−15.32 and − 15.40 kcal/mol) than the anticancer drug sorafenib (−13.59 kcal/mol), with **7h** achieving the most favorable MM-GBSA energy (−105.03 kcal/mol). These findings suggest that **6h** and **7h** may act as dual-function agents, effectively targeting both cholinesterase enzymes and oncogenic YAP–TEAD1 signaling, with potential therapeutic relevance for neurodegenerative diseases and neuroblastoma.

2.5.1. Molecular docking ligand protein interaction analysis on AChE

Molecular docking, 2D and 3D ligand protein interaction analysis, and binding modes of AChE with **6h** and **7h** are given in Fig. 3.

In Fig. 3**a**, the thiosemicarbazide moiety of compound **6h** forms hydrogen bonds through both of its amide nitrogen atoms with Tyr-337. An additional hydrogen bond is observed between the imine nitrogen and Tyr-124. Furthermore, compound **6h** establishes four distinct π–π stacking interactions with the active site of AChE. The indole ring forms three π–π stacking interactions with Tyr-341 and Tyr-124, while the phenylsulfonyl ring engages in one π–π stacking interaction with Tyr-72. In Fig. 3**b**, compound **7h** exhibits a similar binding pattern to **6h**. Its thiosemicarbazide moiety also forms hydrogen bonds via both amide nitrogen atoms with Tyr-337, and an additional hydrogen bond is observed between the imine nitrogen and Tyr-124. Beyond these hydrogen bonds, compound **7h** engages in four π–π stacking interactions: two occur between its fluorophenyl ring and Trp-86, and the other two involve the indole ring and Tyr-341.

Fig. 3c and **d** display the 3D ligand–protein interaction (LPI) diagrams and binding modes of **6h** and **7h**, respectively, within AChE. In these figures, yellow dashes represent hydrogen bonds, while turquoise lines indicate π–π stacking interactions. The gray cloud-like surface illustrates the binding surface area of the protein, and the blue surface represents the ligand's binding interface. The degree of fit between these two surfaces indicates how well the ligand occupies the binding site. As observed in both 3D figures, the ligand and protein binding surfaces

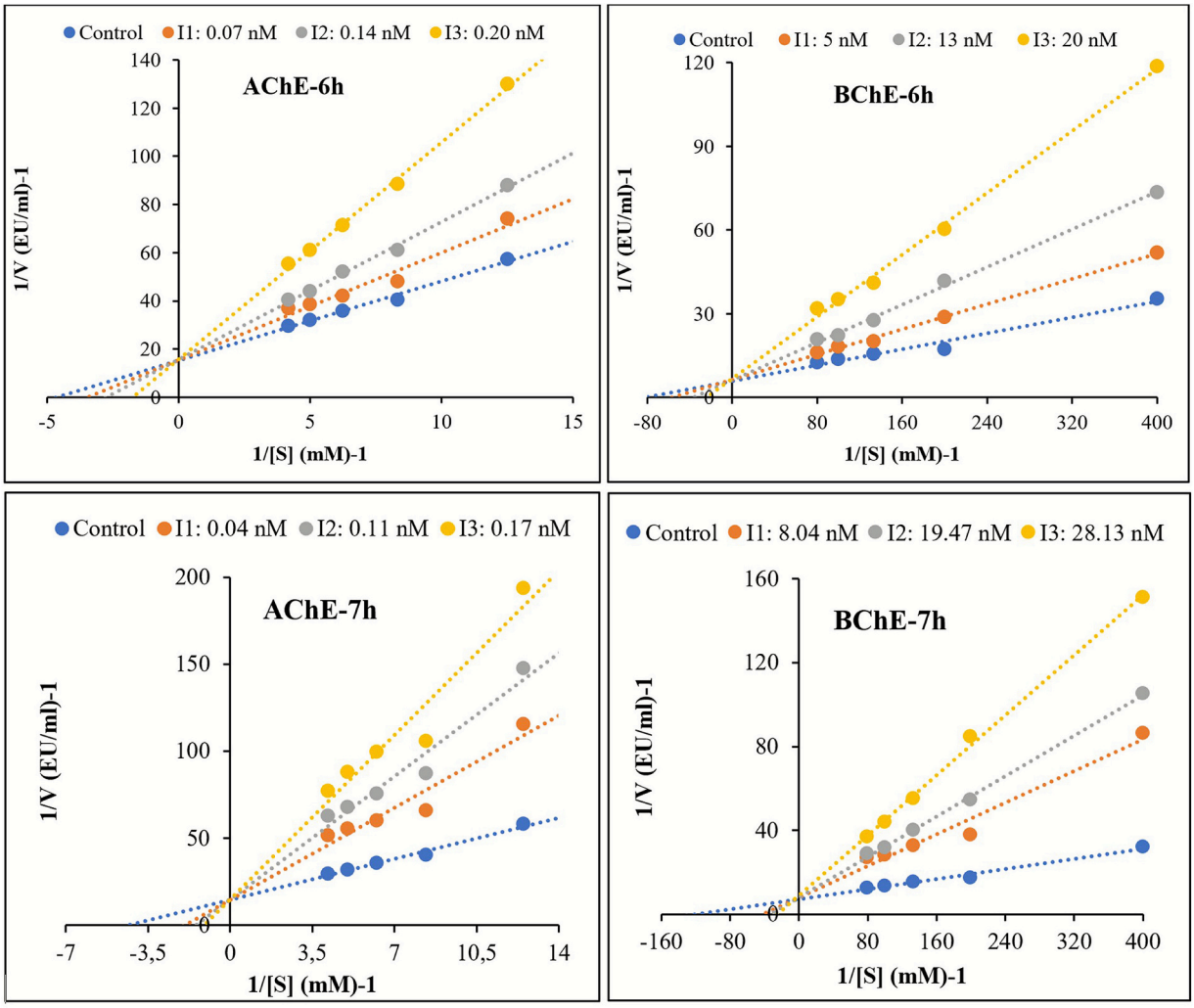

Fig. 2. K_i graphs of the most active compounds **6 h** and **7 h** against AChE and BChE.

Table 2
IC_{50} values (μM) of the compounds on SH-SY5Y and CCD-1079Sk cell lines.

Title	IC_{50} [μM] SH-SY5Y	CCD-1079Sk	SI
6a	4.49 ± 0.02	18.51 ± 0.05	4.1
6b	1.53 ± 0.02	22.34 ± 0.05	14.6
s6c	2.60 ± 0.02	20.44 ± 0.05	7.9
6d	2.74 ± 0.02	22.20 ± 0.05	8.1
6e	2.38 ± 0.02	30.32 ± 0.06	12.7
6f	0.92 ± 0.01	29.27 ± 0.04	31.8
6g	1.48 ± 0.01	20.13 ± 0.05	13.6
6h	**0.51 ± 0.01**	**64.52 ± 0.05**	**126.5**
6i	2.13 ± 0.02	28.66 ± 0.06	13.5
6j	0.66 ± 0.01	17.16 ± 0.04	26.0
7b	2.18 ± 0.02	22.22 ± 0.05	10.2
7c	3.82 ± 0.02	18.96 ± 0.03	5.0
7d	4.89 ± 0.03	32.55 ± 0.05	6.7
7e	2.05 ± 0.02	18.72 ± 0.06	9.1
7f	1.54 ± 0.01	35.35 ± 0.03	23.0
7g	2.29 ± 0.02	43.89 ± 0.04	19.2
7h	**0.87 ± 0.01**	**52.35 ± 0.05**	**60.1**
7i	2.20 ± 0.02	27.36 ± 0.02	12.4
7j	0.91 ± 0.01	45.14 ± 0.07	49.6
Srf*	3.82 ± 0.02	17.88 ± 0.04	4.7

* Srf = Sorafenib was used as a reference drug.

align closely, suggesting an excellent fit within the active site. In the **6h–AChE** complex, hydrogen bond lengths range from 1.92 to 2.22 Å, and π–π stacking interactions span 3.91 to 5.48 Å.

In the **7h–AChE** complex, hydrogen bond lengths are between 1.94 and 2.30 Å, and π–π stacking interactions range from 3.70 to 4.36 Å. The short hydrogen bond lengths indicate strong interactions within the binding site. Both ligand–protein complexes are stabilized by multiple strong hydrogen bonds and π–π stacking interactions, forming robust and stable complexes.

The docking results revealed that compounds **6h** and **7h** interact with key residues in both the catalytic active site (CAS), including Trp-86, Phe-295, Phe-297, Tyr-337, and His-447, and the peripheral anionic site (PAS) comprising Tyr-72, Tyr-124, Trp-286, and Tyr-34, of AChE. Compound **6h** forms hydrogen bonds with Tyr-337 and Tyr-124 and establishes multiple π–π stacking interactions with Tyr-341, Tyr-124, and Tyr-72. Similarly, **7h** interacts via hydrogen bonds with Tyr-337 and Tyr-124 and engages in π–π stacking with Trp-86 and Tyr-341. These interactions suggest a possible dual-site binding mode extending from the CAS toward the PAS. However, enzyme kinetic results showing competitive inhibition indicate that the main interaction occurs at the CAS region, while PAS contacts may contribute to additional stabilization within the active-site.

2.5.2. Molecular docking ligand protein interaction analysis on BChE

Molecular docking 2D and 3D ligand protein interaction analysis and binding modes of BChE with **6h** and **7h** are given in Fig. 4.

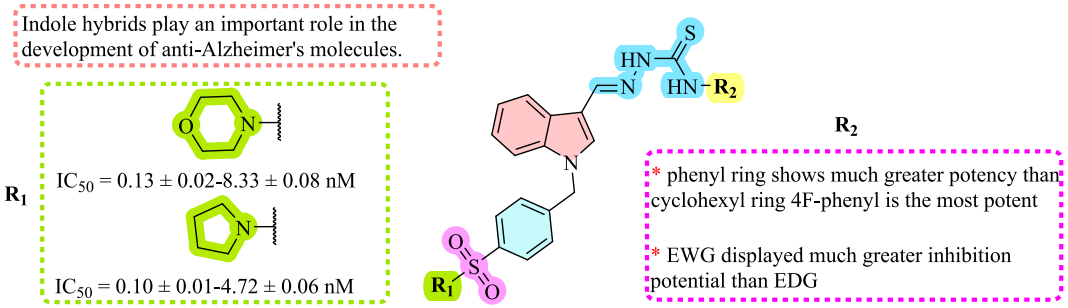

Scheme 3. SAR illustrations of the synthesized compounds as AChE/BChE inhibitors.

Table 3
Molecular docking scores and MM-GBSA binding free energies of the most active compounds and reference drugs against target proteins.

Compounds	Docking score (kcal/Mol)			MM-GBSA ΔG bind. (kcal/Mol)		
	AChE	BChE	Yap-Tead1	AChE	BChE	Yap-Tead1
6h	−12.50	−11.73	−15.32	−83.06	−71.32	−95.98
7h	−11.38	−11.21	−15.40	−69.65	−76.38	−105.03
Tacrine	−10.53	−7.50	–	−55.36	−46.87	–
Galantamine	−7.377	−6.23	–	−51.46	−57.53	–
Sorafenib	–	–	−13.59	–	–	−97.92

In Fig. 4**a**, the 2D ligand–protein interaction (LPI) diagram of the **6h–BChE** complex shows that the sulfur atom of the thiosemicarbazide group forms a strong and directional hydrogen bond with Glu-197, contributing significantly to complex stability. Additionally, a π–π stacking interaction is observed between the fluorophenyl ring and Trp-82, while the indole ring participates in three π–π stacking interactions with Trp-231 and Phe-329. In Fig. 4**b**, the 2D LPI diagram of the **7h–BChE** complex reveals a similar binding mode. The sulfur atom of the thiosemicarbazide group forms two hydrogen bonds with Glu-197 and Glu-116, which play a key role in anchoring the ligand within the active site. A π–π stacking interaction occurs between the fluorophenyl ring and Trp-82, while the indole ring engages in three π–π stacking interactions with Trp-231 and Phe-329.

Fig. 4**c** and **d** illustrate the 3D ligand–protein interaction maps and binding conformations of **6h** and **7h** with BChE. In the **6h–BChE** complex, the hydrogen bond length is 2.75 Å, consistent with a strong and stabilizing interaction. In the **7h–BChE** complex, two hydrogen bonds are observed at 2.49 Å and 2.52 Å, further reinforcing the ligand's binding affinity. The π–π stacking interaction distances range from 3.83 to 5.42 Å in both complexes. In both complexes, the ligand and protein binding surfaces align well, indicating an excellent fit in the active site. However, in the **7h–BChE** complex, the pyrrolidine ring shows minimal solvent exposure.

In summary, molecular docking studies revealed that both compounds **6h** and **7h** exhibit strong and consistent binding interactions with AChE, BChE, and YAP–TEAD1, primarily through their thiosemicarbazide groups, which formed key hydrogen bonds with conserved residues such as Tyr-337, Glu-197, and Pro-357/Ser-310. The indole ring in both ligands engaged in recurrent π–π stacking interactions with aromatic residues like Tyr-341, Phe-221, and Phe-329, contributing to binding stability. Additionally, **7h** showed unique π–cation interaction with Lys-336, and generally exhibited deeper binding and lower solvent exposure compared to **6h**. The high surface complementarity and short interaction distances in all complexes suggest that both ligands adopt favorable conformations, supporting their potential as multi-target inhibitors with a shared pharmacophore framework.

2.6. Molecular dynamics (MD) simulations

Molecular dynamics (MD) simulations were carried out to evaluate the complex stabilities of 6h–AChE, 7h–AChE, 6h–BChE, and 7h–BChE ligand–protein complexes. Additionally, the Yap–TED1 complexes were included in the Supplementary Data. The simulation results were evaluated by analyzing both RMSD and RMSF plots. RMSD analysis was used to assess the overall structural stability of the complexes over time, with lower RMSD values indicating greater conformational stability. RMSF analysis, on the other hand, was performed to investigate the flexibility and mobility of individual amino acid residues, where higher RMSF values suggest more dynamic regions within the protein structure [67].

2.6.1. MD simulation analysis on AChE

MD simulation analyses of the **6h–AChE** complex are presented in Fig. 5.

Fig. 5**a** illustrates the 2D key ligand-protein interaction diagram of the **6h–AChE** complex obtained from MD simulation, along with interaction percentages. Notably, the nitrogen atoms of the thiosemicarbazide moiety in compound **6h** formed hydrogen bonds with Tyr-337 for 70 % and 60 % of the simulation time, respectively (purple arrows). In addition, the same moiety established two weaker hydrogen bonds with Tyr-124, maintained for 23 % and 7 % of the simulation duration. The complex also exhibited a total of six π–π stacking interactions. Among these, the most dominant was between the fluorophenyl ring and Trp-86, which persisted for 94 % of the simulation time, marked by green lines. This strong aromatic interaction likely plays a major role in stabilizing the ligand in the binding pocket. Additionally, the indole ring formed π–π stacking interactions with Tyr-341 and Tyr-124 for 68 % and 41 % of the simulation time, respectively, further contributing to the overall binding stability.

Fig. 5**b** presents the RMSD plots of the protein Cα atoms and the ligand throughout the 250 ns simulation of **6h-AChE** complex. The average RMSD for the protein backbone was 1.2 Å (pale blue), indicating a stable protein conformation. The ligand RMSD, when aligned to the protein, was measured as 2.4 Å (red), while the internal ligand RMSD (fit on ligand) was 1.6 Å (pink), suggesting moderate flexibility but overall retained conformation during the simulation. Fig. 5**c** shows the ligand RMSF analysis. Both the ligand-fit-on-protein and ligand-fit-on-ligand RMSF values averaged around 1.0 Å, indicating minimal atomic fluctuations and a relatively rigid ligand conformation throughout the simulation, which supports its strong and stable binding. Fig. 5**d** displays the fractional interaction histogram of the **6h–AChE** complex. In an MD simulation, a functional group may interact with multiple amino acid residues, and conversely, a single residue can interact with multiple ligand groups. Therefore, fractional interactions are summed to generate a histogram. In the plot, green bars represent hydrogen bonds, blue bars indicate water-bridged hydrogen bonds, and purple bars show hydrophobic interactions. According to the histogram, key interacting residues include Tyr-124, Tyr-337, Tyr-341, and Trp-86, all of which played significant roles in ligand stabilization through various non-covalent interactions.

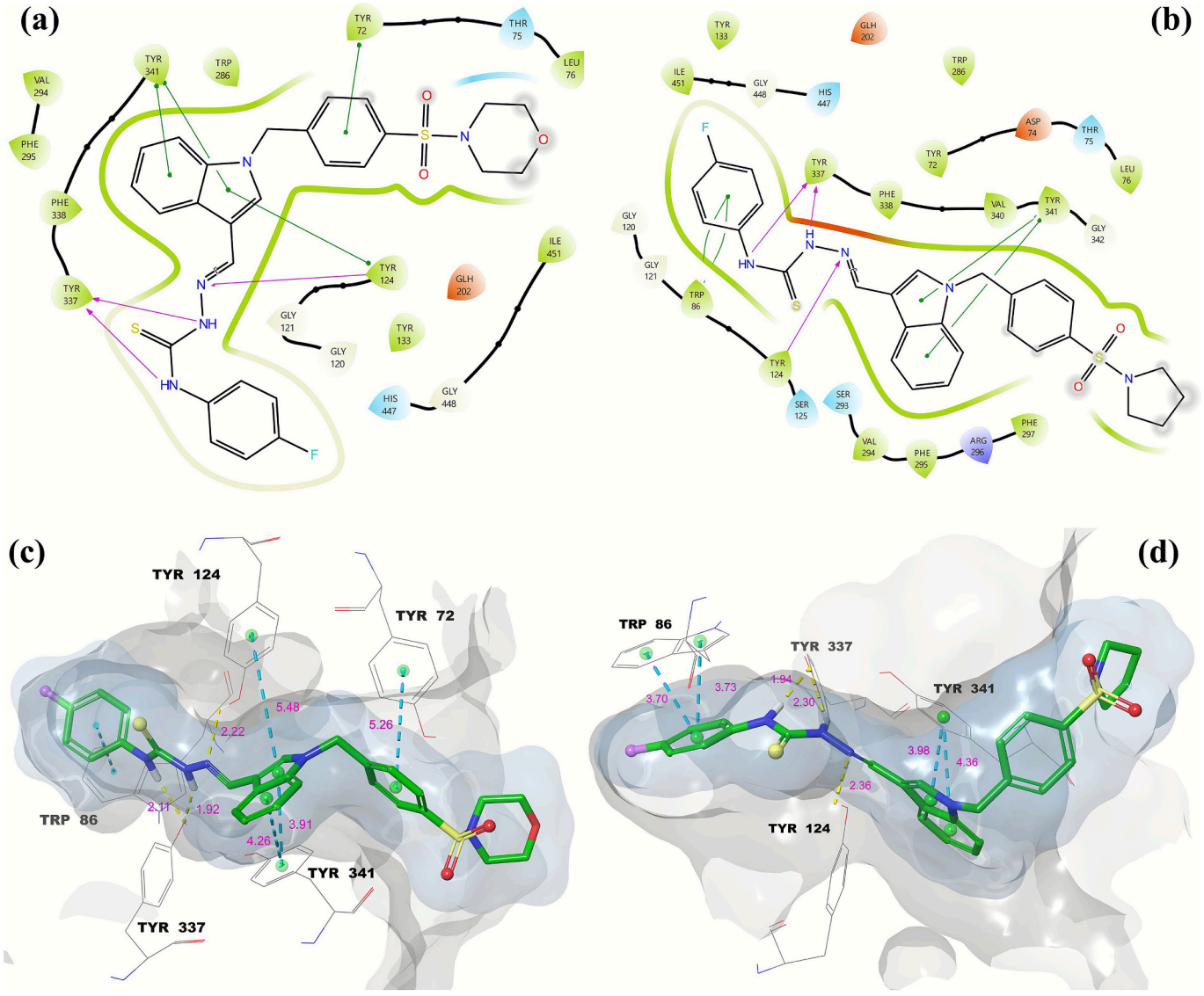

Fig. 3. Molecular docking, 2D and 3D ligand protein interaction analysis, and binding modes of AChE with **6 h** and **7 h.**

MD simulation analyses of the **7h–AChE** complex is presented in Fig. 6. Fig. 6**a** illustrates the 2D key protein-ligand interactions throughout the MD simulation. Similar to compound **6h**, the thiosemicarbazide moiety of **7 h** formed three distinct hydrogen bonds with Tyr-337 and Tyr-124, persisting for 57 %, 57 %, and 59 % of the simulation time, respectively. The fluorophenyl ring exhibited a strong and highly persistent π–π stacking interaction with Trp-86, lasting for 97 % of the simulation duration. This dominant interaction plays a critical role in maintaining the stability of the protein-ligand complex and highlights the functional significance of this aromatic group in binding affinity. In addition, the indole ring of **7h** formed a secondary π-π stacking interaction with Tyr-341, sustained for 82 % of the simulation time, further reinforcing the ligand's stable positioning within the active site.

Fig. 6**b** shows the RMSD plots of the protein Cα atoms and ligand. The average RMSD values were 1.2 Å for the protein backbone (pale blue), 2.3 Å for the ligand aligned to the protein (red), and 2.0 Å for the internal ligand alignment (pink). These values indicate that the protein remained structurally stable during the 250 ns simulation, while the ligand exhibited a modest degree of internal flexibility yet preserved its binding orientation. Fig. 6**c** displays the RMSF values of the ligand atoms. Both the ligand-fit-on-protein and ligand-fit-on-ligand RMSF values were around 1.0 Å on average, suggesting minimal atomic fluctuations and overall high conformational stability of the ligand within the binding site. Fig. 6**d** presents the fractional interaction histogram for the **7h-AChE** complex. As in Fig. 6**d**, this analysis reflects cumulative interactions between ligand functional groups and protein residues over the entire simulation. Key interacting residues that emerged prominently include Tyr-341, Tyr-337, Trp-86, Tyr-124, and Trp-286. These residues engaged in hydrogen bonding, water-mediated hydrogen bonds, and hydrophobic interactions, all contributing to the stability and affinity of the complex.

As a result, the MD simulation analyses demonstrate that both compounds **6h** and **7h** maintain stable binding poses within the AChE active site throughout the simulation. This stability is supported by persistent hydrogen bonding involving the thiosemicarbazide moiety and extensive π–π stacking interactions between aromatic rings, particularly the fluorophenyl and indole groups, and key residues Trp-86 and Tyr-341. The consistently low RMSD and RMSF values observed for both ligand and protein confirm the structural integrity of these complexes, reinforcing the potential of **6h** and **7h** as strong AChE inhibitors and highlighting the critical role of these functional groups and π-π stacking interactions in ligand binding stability.

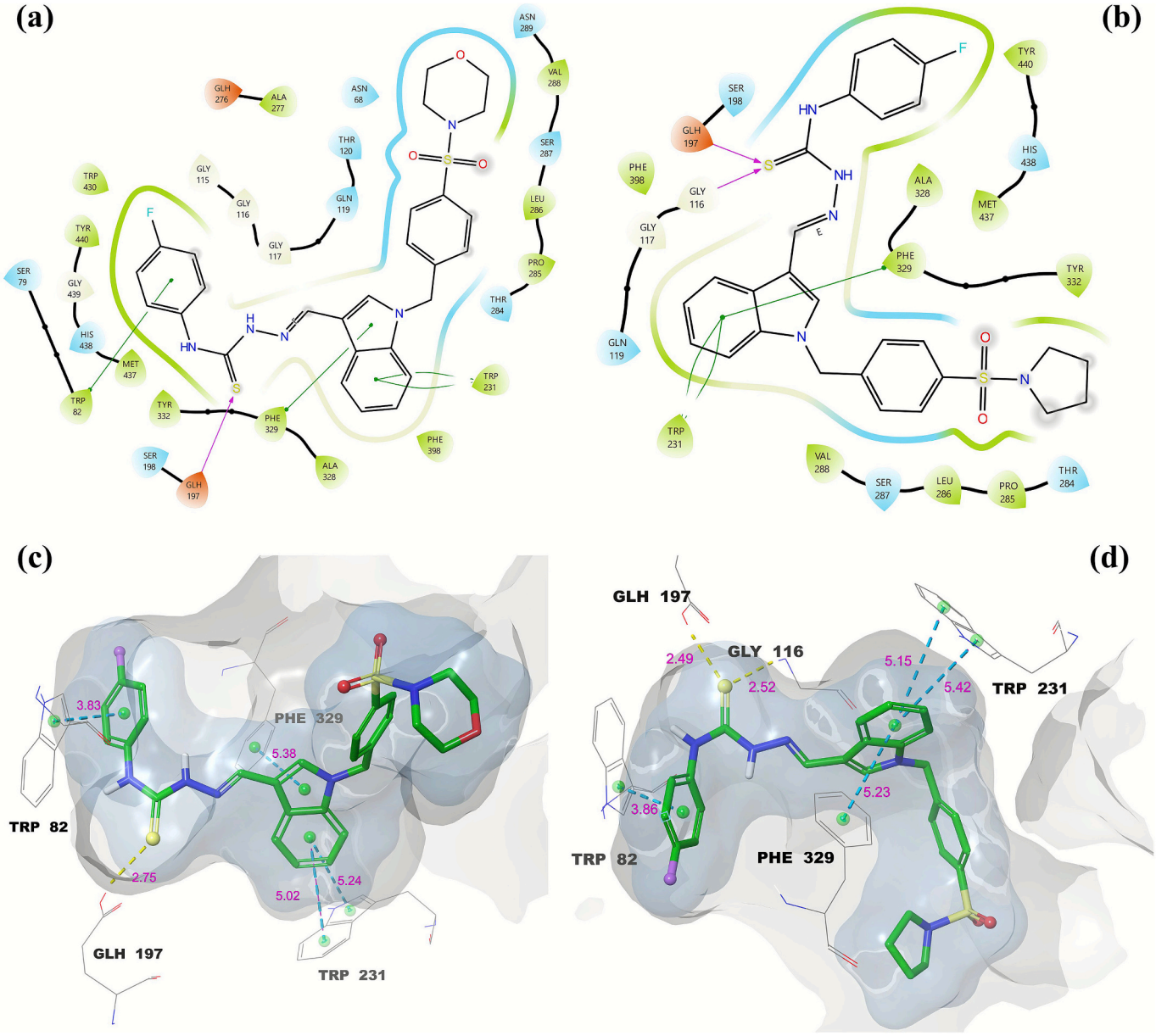

Fig. 4. Molecular docking 2D and 3D LPI analysis and binding modes of BChE with **6 h** and **7 h.**

2.6.2. MD simulation analysis on BChE

MD simulation analysis of the **6h-BChE** complex is presented in Fig. 7. Fig. 7**a** illustrates the 2D key ligand-protein interactions observed during the simulation. The sulfur atom of the thiosemicarbazide ring formed a hydrogen bond with Glu-197 for 65 % of the simulation time. The sulfonamide group engaged in a water-bridged hydrogen bond interaction with Gln-71 for 35 % of the simulation. Similar to the AChE complexes, the fluorophenyl ring played a prominent role by establishing a π–π stacking interaction with Trp-82, maintained for 78 % of the simulation. The indole ring also contributed to binding stability through π-π stacking interactions with Phe-329 and Trp-231 for 61 % and 47 % of the simulation time, respectively.

Fig. 7**b** shows the RMSD plots of protein Cα and ligand atoms of **6h-BChE** complex. The average protein Cα RMSD was 1.2 Å (pale blue), while the average ligand RMSD aligned on the protein was 1.5 Å (red). The internal ligand RMSD (ligand fit on ligand) was measured as 0.9 Å (pink), indicating minimal internal fluctuations. Fig. 7**c** presents the RMSF values of the ligand atoms, with an average of approximately 0.85 Å, reflecting low atomic mobility. Finally, Fig. 7**d** displays the fractional interaction histogram, highlighting Phe-329 and Trp-82 as key interacting residues, followed by Glu-197 and Trp-231, which also contributed significantly to ligand stabilization.

MD simulation analysis of the **7h-BChE** complex is presented in Fig. 8.

Fig. 8**a** presents the 2D key ligand-protein interactions of the **7h-BChE** complex throughout the 250 ns MD simulation. A large number of hydrogen bonds and water-bridged hydrogen bonds are observed, which play a critical role in the stability of the ligand-protein complex. The sulfur atom of the thiosemicarbazide group formed two hydrogen bonds with Gly-116 (20 %) and Tyr-128 (22 %) of the simulation time, while the sulfonyl group engaged in three distinct water-bridged hydrogen bonds with Asp-70 and Asn-68. The indole ring contributed to the complex stability via three different π-π stacking interactions: two with Phe-329 at 63 % and 25 %, and one with Trp-231 at 46 % of the simulation duration. Fig. 8**b** shows the RMSD plots of the protein and ligand atoms. The average RMSD values during the simulation were 1.2 Å for the protein Cα atoms (pale blue), 2.1 Å for the ligand aligned on the protein (red), and 1.8 Å for the internal ligand alignment (pink). Fig. 8**c**

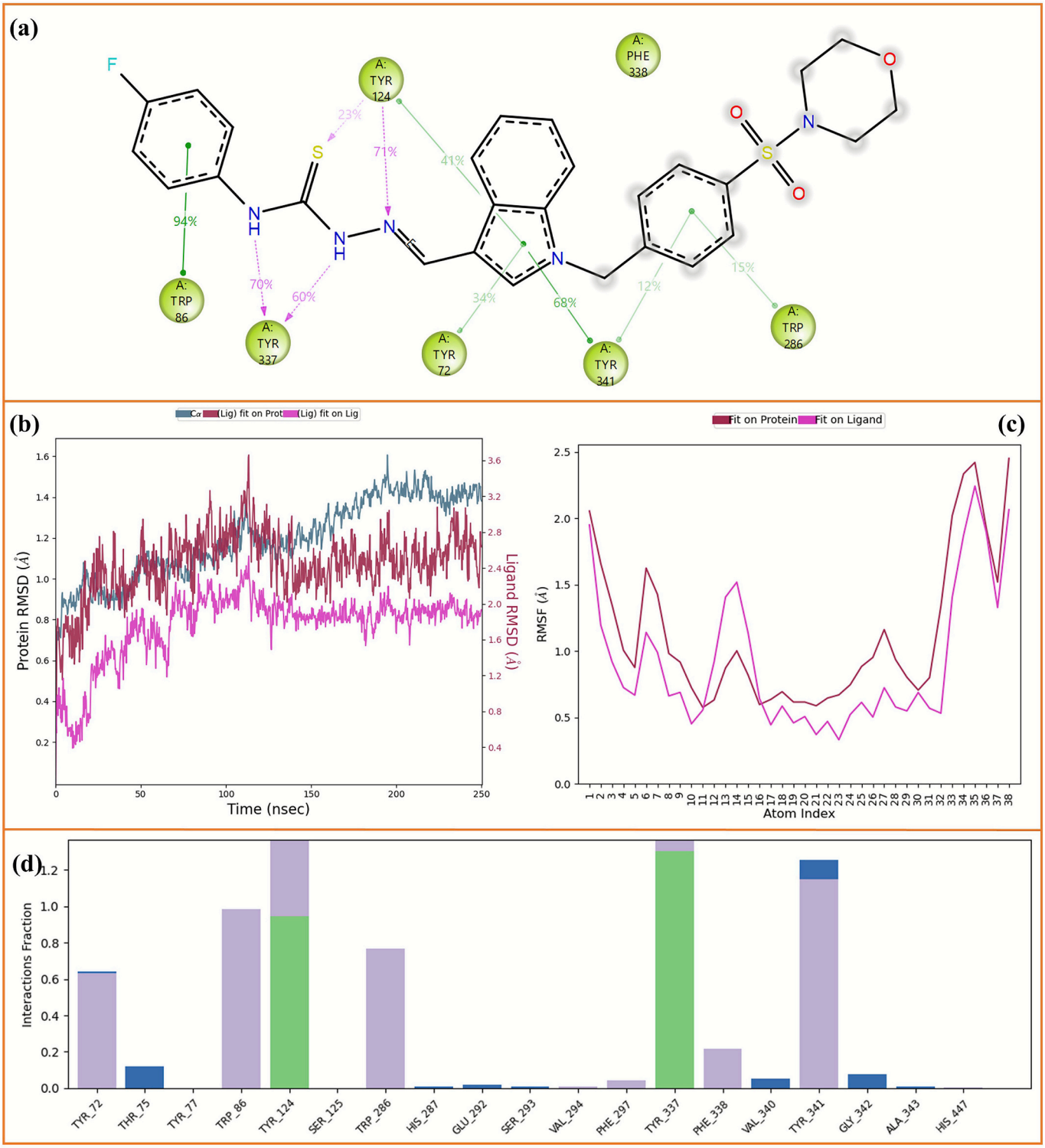

Fig. 5. The 250 ns MD simulation analysis of **6h-AChE** complex. (a) 2D key ligand protein interactions, (b) RMSD values of protein and ligand atoms, (c) RMSF values of ligand atoms, (d) fractional interaction histogram.

presents the ligand RMSF values, with an average around 1.0 Å, indicating low atomic fluctuations and high stability. Finally, Fig. 8**d** displays the fractional interaction histogram, highlighting Pro-329, Trp-82, Asn-68, Asp-70, and Trp-231 as key residues involved in the majority of interactions with the ligand.

The MD simulation analyses of the **6h-BChE** and **7h-BChE** complexes demonstrate stable ligand binding throughout the 250 ns simulation period. Both compounds maintained persistent hydrogen bonding and water-bridged interactions primarily involving the thiosemicarbazide sulfur atom and sulfonyl groups with key residues such as Glu-197, Gln-71, Asp-70, and Asn-68. Additionally, extensive π–π stacking interactions involving the fluorophenyl and indole rings with aromatic residues including Trp-82, Phe-329, Trp-231, and Pro-329 contributed significantly to complex stability. The low RMSD and RMSF values for both protein and ligand atoms further confirm the structural integrity and minimal flexibility of the complexes, supporting

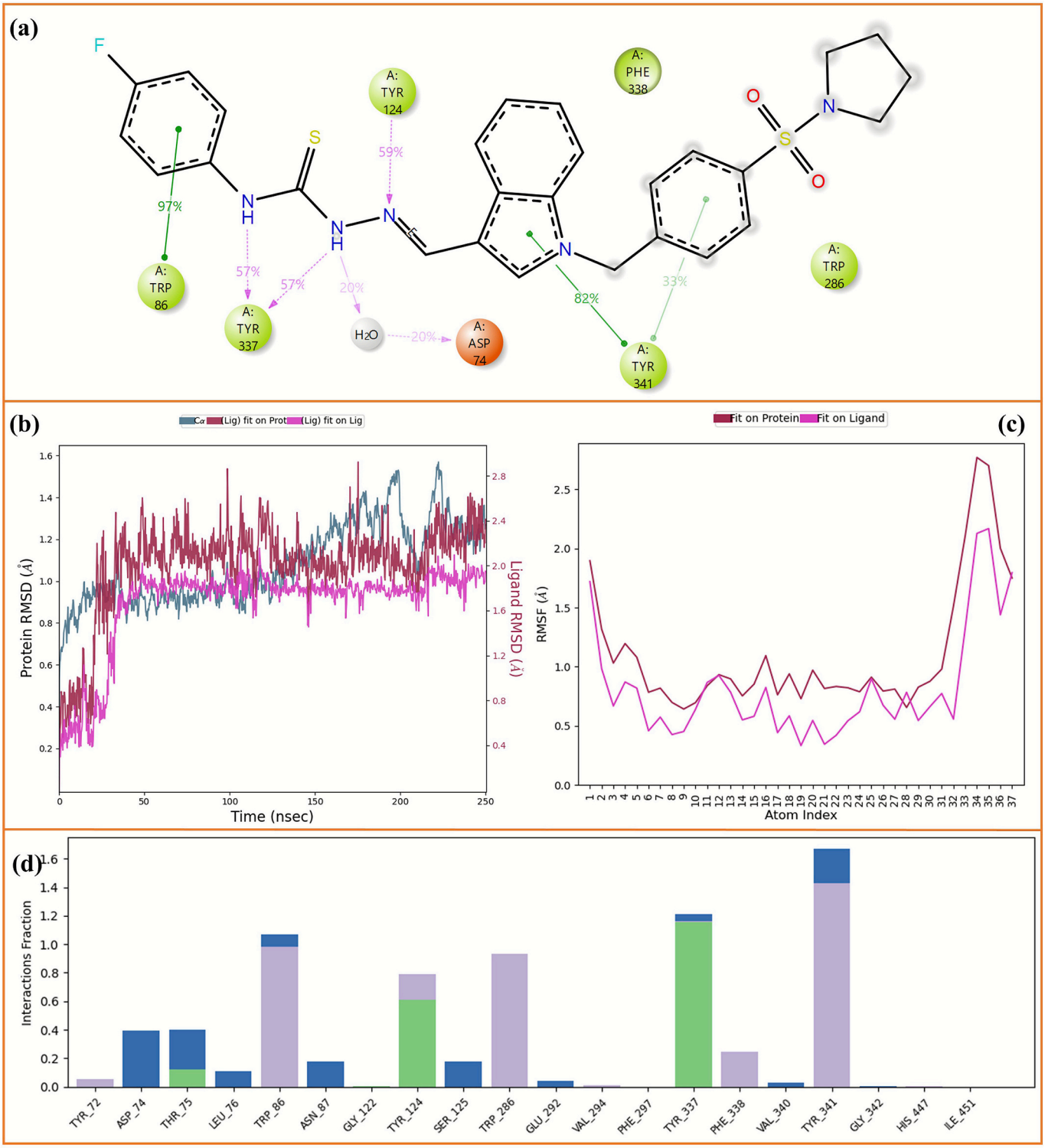

Fig. 6. The 250 ns MD simulation analysis of **7h-AChE** complex. (a) 2D key ligand protein interactions, (b) RMSD values of protein and ligand atoms, (c) RMSF values of ligand atoms, (d) fractional interaction histogram.

the potential of compounds **6h** and **7h** as effective BChE inhibitors.

2.7. ADME prediction

To assess the drug-likeness and preliminary safety of the synthesized compounds, in silico ADME (absorption, distribution, metabolism, excretion) predictions were performed. These analyses provide insight into the pharmacokinetic properties and potential toxicity of the molecules, guiding further optimization and future in vivo studies. The results are given in Table 4.

The ADME predictions of the synthesized compounds given in Table 4 indicate generally favorable drug-like properties. Molecular weights are within an acceptable range, and the number of hydrogen bond donors *(dHB)* and acceptors *(aHB)* comply with Lipinski's rules *(Ro5 ≤ 4)*. Most compounds show good intestinal permeability (QPPCaco >500) and high predicted oral absorption *(%HOA > 80)*,

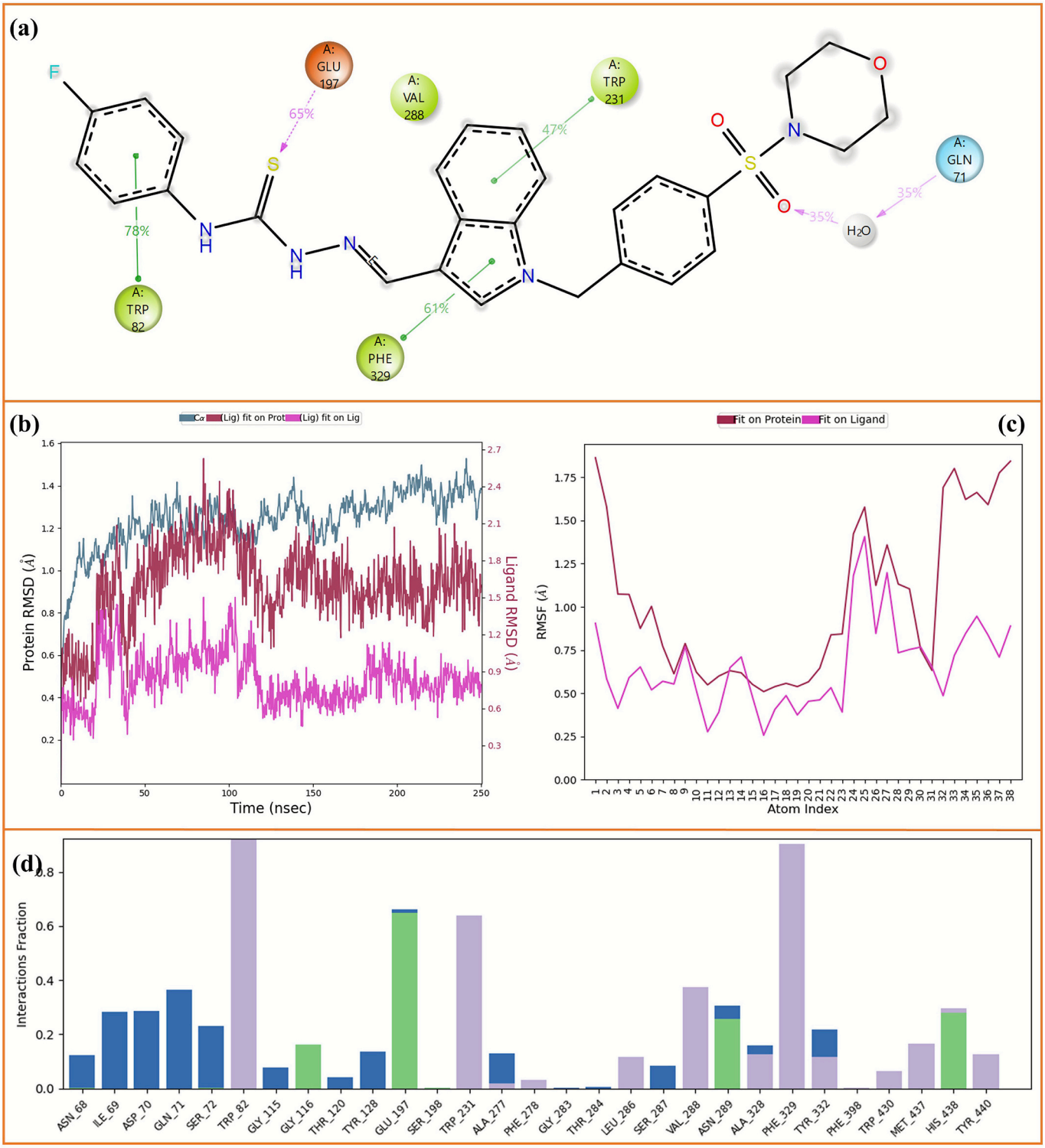

Fig. 7. The 250 ns MD simulation analysis of **6h-BChE** complex. (a) 2D key ligand protein interactions, (b) RMSD values of protein and ligand atoms, (c) RMSF values of ligand atoms, (d) fractional interaction histogram.

although a few compounds (**6e, 6f, 7e, 7f**) have lower values. The octanol/water partition coefficients (QPlogPo/w) suggest balanced lipophilicity and predicted aqueous solubility *(QPlogS)* falls mostly within the acceptable range. Blood–brain barrier penetration *(QPlogBB, QPPMDCK)* varies, with some compounds showing moderate CNS penetration potential. Overall, the predicted ADME profiles support the further development of these hybrids as bioactive molecules with reasonable pharmacokinetic properties.

2.8. Toxicity prediction

In silico toxicity prediction plays a crucial role in the early stages of drug discovery to evaluate the safety profile of newly designed compounds before experimental testing. Computational models can estimate organ-specific toxicities such as hepatotoxicity, nephrotoxicity, neurotoxicity, and cardiotoxicity, as well as toxicity end points including mutagenicity, cytotoxicity, and carcinogenicity. These parameters

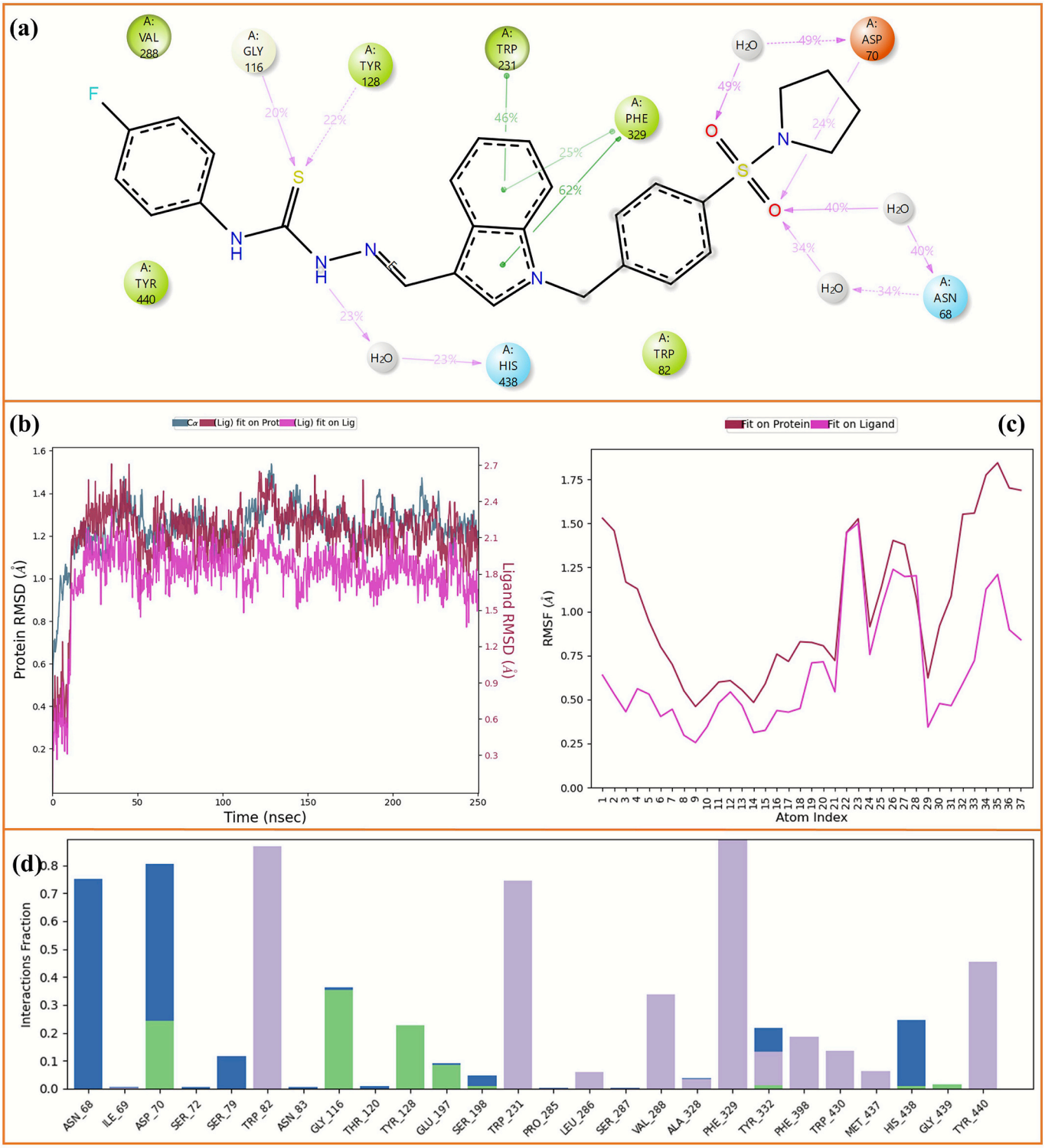

Fig. 8. The 250 ns MD simulation analysis of **7h-BChE** complex. (a) 2D key ligand protein interactions, (b) RMSD values of protein and ligand atoms, (c) RMSF values of ligand atoms, (d) fractional interaction histogram.

provide insight into the potential adverse effects that may limit clinical applicability.

Furthermore, predicted LD_{50} values and toxicity classes serve as general indicators of acute toxicity, allowing classification according to the Globally Harmonized System (GHS), where lower class numbers correspond to higher toxicity. The overall prediction accuracy indicates the reliability of the applied computational model. Prediction results are given in Table 5.

The predicted toxicity analysis revealed that none of the tested compounds exhibited nephrotoxicity or cardiotoxicity, indicating a favorable safety profile regarding renal and cardiac functions. However, some derivatives **(6e–6h** and **6j)** showed hepatotoxic potential, suggesting possible liver-related adverse effects, while neurotoxicity was observed for compounds **6c, 6j, 7a–7d, 7h,** and **7j.** Regarding the toxicity endpoints, carcinogenicity was predicted for compounds **6d–6g, 6i, 7e, 7f,** and **7i**, and mutagenicity was observed for **6e, 6f, 7e,** and **7f,**

Table 4
ADME prediction of title compounds.*

Title	MW	dHB	aHB	QPlogPo/w	QPlogS	QPPCaco	QPlogBB	QPPMDCK	%HOA	Ro5	Ro3
6a	471.59	2	10	3.609	−5.921	809	−0.934	996	100	0	1
6b	539.70	2	10	5.151	−7.816	1131	−0.922	1428	85	2	1
6c	582.13	2	10	5.690	−7.768	1201	−0.728	3767	89	2	1
6d	547.68	2	10	5.178	−7.993	845	−1.171	805	83	2	1
6e	578.66	2	11	4.010	−6.734	99	−2.298	59	60	2	1
6f	578.66	2	11	4.144	−7.458	100	−2.403	80	61	2	1
6g	563.68	2	11	4.949	−7.541	868	−1.196	841	95	1	1
6h	551.65	2	10	5.091	−7.618	869	−0.988	1521	83	2	1
6i	561.71	2	10	5.485	−8.048	1262	−0.937	1159	88	2	1
6j	602.55	2	10	5.759	−8.441	1007	−0.758	4265	88	2	1
7a	547.68	2	9	5.812	−8.819	797	−1.342	727	86	2	1
7b	523.71	2	9	5.764	−8.424	1118	−0.950	1328	89	2	1
7c	566.13	2	9	6.526	−9.287	1028	−0.938	2988	93	2	1
7d	545.71	2	9	6.163	−8.568	1029	−1.057	1219	91	2	1
7e	562.66	2	10	4.882	−8.461	90	−2.549	77	77	1	1
7f	562.66	2	9	4.826	−8.387	93	−2.542	75	77	1	1
7g	547.68	2	9	5.677	−8.451	779	−1.283	801	86	2	1
7h	535.65	2	9	5.768	−8.504	812	−1.072	1427	86	2	1
7i	545.71	2	9	6.040	−8.660	998	−1.080	882	90	2	1
7j	586.55	2	9	6.444	−9.369	932	−0.848	3964	91	2	1

* **MW** 130 to 725 (molecular weight); **dHB** 0 to 6 (H-bond donors); **aHB** 2 to 20 (H-bond acceptors); **QPlogPo/w** − 2 to 6.5 (octanol/water partition coefficient); **QPlogS** –6.5 to 0.5 (aqueous solubility, log S); **QPPCaco** < 25 poor, >500 great (intestinal permeability); **QPlogBB** –3 to 1.2 (brain/blood partition); **QPPMDCK** < 25 poor, >500 great (BBB permeability); **%HOA** > 80 high, <25 poor (oral absorption); **Ro5** ≤ 4 (Lipinski); **Ro3** ≤ 3 (Jorgensen).

Table 5
Predicted toxicity parameters.

Parameters*	6a	6b	6c	6d	6e	6f	6 g	6 h	6i	6j	7a	7b	7c	7d	7e	7f	7 g	7 h	7i	7j
Hepatotoxicity	−	−	−	−	+	+	+	+	−	+	−	−	−	−	−	−	−	−	−	−
Neurotoxicity	−	−	+	−	−	−	−	−	−	+	+	+	+	+	−	−	−	+	−	+
Nephrotoxicity	−	−	−	−	−	−	−	−	−	−	−	−	−	−	−	−	−	−	−	−
Cardiotoxicity	−	−	−	−	−	−	−	−	−	−	−	−	−	−	−	−	−	−	−	−
Carcinogenicity	−	−	−	+	+	+	+	−	+	−	−	−	−	−	+	+	−	−	+	−
Cytotoxicity	−	−	−	−	−	−	−	−	−	−	−	−	−	−	−	−	−	−	−	−
Mutagenicity	−	−	−	−	+	+	−	−	−	−	−	−	−	−	+	+	−	−	−	−
Pred. LD_{50} (g/kg)	2.5	2.5	2.5	3.8	5.0	5.0	10.0	3.8	5.0	0.008	0.42	1.0	0.3	3.8	3.8	3.8	10.0	3.8	3.8	0.008
Pred. Tox. Class	5	5	5	5	5	5	6	5	5	2	4	4	3	5	5	5	6	5	5	2
Tox. Pred. Accur. (%)	54	54	54	54	23	54	54	54	54	54	54	54	54	54	54	54	54	54	54	54

* (-) = negative, no toxicity; (+) = positive, toxic

which may indicate potential genotoxic risks. Importantly, none of the compounds showed cytotoxicity, implying good selectivity and low nonspecific toxicity. The predicted LD_{50} values varied widely from 0.008 to 10.0 g/kg, with most compounds belonging to toxicity class 5, indicating low acute toxicity, while compounds **6j** and **7j** (class 2) exhibited comparatively higher toxicity. In contrast, derivatives such as **6g** and **7g** were classified as class 6, representing minimal toxicity. Overall, the prediction model demonstrated moderate reliability with an accuracy of approximately 54 %, supporting the need for further experimental validation to confirm these computational toxicity findings.

3. Conclusions

In this study, 20 novel morpholino/pyrrolidino-sulfonyl-indole thiosemicarbazone derivatives (**6a–j** and **7a–j**) were synthesized and evaluated for cholinesterase inhibition and anticancer activities. Compounds **6h** and **7h** emerged as the most potent inhibitors of AChE and BChE, with IC_{50} values as low as 0.15 μM and 0.12 μM, respectively, surpassing reference drugs. They also showed promising cytotoxicity against SH-SY5Y neuroblastoma cells (IC_{50} = 3.8 μM for **6h**, 4.2 μM for **7h**) with high selectivity indices (SI = 126 for **6h**, SI = 60 for **7h**), highlighting their therapeutic potential.

Molecular docking and MM-GBSA calculations revealed strong and stable interactions within the active sites of AChE and BChE (Glide XP scores −8.7 to −9.3 kcal/mol; ΔG bind −55 to −62 kcal/mol), with key residues forming persistent hydrogen bonds and π–π stacking. Molecular dynamics simulations over 250 ns confirmed structural stability, minimal conformational fluctuations, and sustained ligand–protein interactions. ADMET predictions indicated generally favorable pharmacokinetic properties and acceptable toxicity profiles, supporting their potential as safe and effective candidates. Collectively, these results demonstrate that **6h** and **7h** are promising multitarget agents with potent cholinesterase inhibitory and anticancer properties for further preclinical development.

4. Experimental section

4.1. General

For the synthesis of 1-morpholinosulphonyl indole-based thiosemicarbazones **6(a-j)** and 1-pyrrolidinosulphonyl indole-based thiosemicarbazones **7(a-j),** all the raw materials were purchased from Sigma-Aldrich. Chemicals and solvents, including indole-3-carbaldehyde, 1-pyrrolidinosulphonyl chloride, 1-morpholinosulphonyl chloride, DCM, ethanol, glacial acetic acid, triethylamine, DMAP, ethyl acetate, and petroleum ether, were purchased from Merck and used in their original form. Silica gel plates with aluminum backs were used to monitor the progress and completion of the reaction. A Bruker Ascend 600 MHz NMR spectrometer was operated to obtain ^{1}H and ^{13}C NMR spectra in DMSO-d_6 at 25 °C (600 MHz for ^{1}H and 150 MHz for ^{13}C). NMR spectra were displayed as chemical shifts (ppm) and coupling constants (*J*) were expressed in Hertz (Hz) to describe signal

multiplicity.

4.2. General procedure for the synthesis of 1-(morpholinosulfonyl)-1H-indole-3-carbaldehyde (3) and 1-(pyrrolidinosulfonyl)-1H-indole-3-carbaldehyde (4)

Indole 3 carbaldehyde (**1**) (2 mmol, 0.29 g) was mixed with a solution of triethyl amine (2.6 mmol, 363 μL), DMAP (2 mmol, 0.245 g), and respective 1-morpholino and 1-pyrrolidinosulphonyl chloride (**2**) (2 mmol, 0.37 g) in DCM (15 mL) under argon atmosphere. The reaction mixture was stirred for 12 h at room temperature. A saturated solution of sodium bicarbonate was added to the reaction mixture. After that, the reaction mixture was extracted with DCM. The combined organic layers were dried, and the solvent was evaporated under a vacuum. The obtained residue of *N*-morpholinosulphonyl indole-3-carbaldehyde (**3**) and *N*-pyrrolidinosulphonyl indole-3-carbaldehyde (**4**) was purified by flash chromatography using a 1:4 solution of ethyl acetate and hexane. The product was obtained with a yield of 94 %.

4.3. General procedure for the synthesis of Thiosemicarbazones 6(a-j) and 7(a-j)

To a solution of respective *N*-substituted sulphonyl chloride (3/4) (1 mmol, 0.1 g) in 10 mL of ethanol, substituted thiosemicarbazides **5(a-j)** were added in equimolar amount (1 mmol) along with a few drops of acetic acid as a catalyst. The reaction mixture was refluxed for 4 h. The reaction progress was monitored by TLC using a 1:5 petroleum ether/ethyl acetate mixture as the eluent. After the reaction was completed, as evidenced by TLC, the precipitates were washed with ethanol and filtered to obtain the targeted thiosemicarbazones **6(a-j)** and **7(a-j)** in excellent to moderate yields.

(E)-N-methyl-2-((1-(4-(morpholinosulfonyl)benzyl)-1*H*-indol-3-yl) methylene)hydrazinecarbothioamide **(6a)**

Color: white; **Yield:** 93 %; **M.P.:** 220–222 °C; **FT-IR (cm^{-1}):** 3388, 3337, 3052, 2903, 1616, 1537, 1511, 1493, 1462, 1410, 1389, 1344, 1256, 1165, 1098, 1015, 972, 808, 733, 560; **^{1}H NMR (600 MHz, DMSO-d_6) δ** 11.21 (1H, s), 8.39–8.29 (2H, m), 8.02 (1H, s), 7.95 (1H, q, J = 4.5 Hz), 7.70 (2H, d, J = 8.0 Hz), 7.47 (3H, dd, J = 19.6, 8.0 Hz), 7.22 (2H, dt, J = 23.2, 7.3 Hz), 5.61 (2H, s), 3.60 (4H, t, J = 4.6 Hz), 3.09 (3H, d, J = 4.6 Hz), 2.82 (4H, t, J = 4.7 Hz); **^{13}C NMR (150 MHz, DMSO-d_6) δ** 177.31, 143.75, 140.24, 137.38, 134.37, 134.06, 128.62, 128.28, 125.07, 123.57, 123.18, 121.59, 111.74, 110.87, 65.70, 49.22, 46.31, 31.54; **ESI-HRMS (*m/z*):** chemical formula: $C_{22}H_{25}N_5O_3S_2$, calcd $[M + H]^+$: 472.14771, found $[M + H]^+$: 472.14684; **HPLC-PDA:** λ 300 nm, MeCN:MeOH (1,1), Rt: 3.80 min, 97.75 %.

(E)-N-cyclohexyl-2-((1-(4-(morpholinosulfonyl)benzyl)-1*H*-indol-3-yl)methylene)hydrazinecarbothioamide **(6b)**

Color: white; **Yield:** 93 %; **M.P.:** 227–229 °C; **FT-IR (cm^{-1}):** 3318, 3136, 2965, 2649, 1603, 1536, 1446, 1385, 1296, 1165, 1066, 939, 812, 73, 615; **^{1}H NMR (600 MHz, DMSO-d_6) δ** 11.29 (1H, s), 8.34 (1H, s), 8.16–8.03 (2H, m), 7.70 (2H, d, J = 8.1 Hz), 7.52 (2H, t, J = 7.2 Hz), 7.45 (3H, d, J = 8.1 Hz), 7.31–7.18 (2H, m), 5.63 (2H, s), 4.20 (1H, dq, J = 9.1, 4.7 Hz), 3.60 (4H, t, J = 4.6 Hz), 2.81 (4H, t, J = 4.6 Hz), 2.04–1.89 (2H, m), 1.72 (2H, dt, J = 13.3, 4.2 Hz), 1.59 (1H, dt, J = 13.2, 4.1 Hz), 1.53–1.30 (4H, m), 1.27 (1H, t, J = 11.7 Hz); **^{13}C NMR (150 MHz, DMSO-d_6) δ** 175.37, 143.71, 140.09, 137.41, 134.36, 134.06, 128.61, 128.24, 125.15, 123.60, 122.06, 121.76, 111.58, 111.23, 65.70, 52.13, 49.25, 46.31, 32.42, 25.57, 24.89; **ESI-HRMS (*m/z*):** chemical formula: $C_{27}H_{33}N_5O_3S_2$, calcd $[M + H]^+$: 540.21031, found $[M + H]^+$: 540.20922; **HPLC-PDA:** λ 300 nm, MeCN:MeOH (1,1), Rt: 4.18 min, 99.52 %.

(E)-N-(4-chlorobenzyl)-2-((1-(4-(morpholinosulfonyl)benzyl)-1*H*-indol-3-yl)methylene)hydrazinecarbothioamide **(6c)**

Color: white; **Yield:** 92 %; **M.P.:** 251–253 °C; **FT-IR (cm^{-1}):** 3341, 3146, 3058, 3007, 2967, 1612, 1549, 1522, 1488, 1464, 1411, 1391, 1296, 1112, 1090, 1051, 969, 804, 783, 607, 557; **^{1}H NMR (600 MHz, DMSO-d_6) δ** 11.38 (1H, s), 8.51 (1H, t, J = 6.3 Hz), 8.37 (1H, s), 8.30 (1H, d, J = 7.9 Hz), 8.05 (1H, s), 7.71 (2H, d, J = 8.1Hz), 7.49 (1 H, d, J = 8.3 Hz), 7.45 (2H, d, J = 8.1 Hz), 7.40 (3H, d, J = 1.9 Hz), 7.23 (1H, t, J = 7.6 Hz), 7.17 (1H, t, J = 7.5 Hz), 5.62 (2H, s), 4.89 (2H, d, J = 6.2 Hz), 3.60 (4H, t, J = 4.7 Hz), 2.82 (4H, t, J = 4.7 Hz); **^{13}C NMR (150 MHz, DMSO-d_6) δ** 177.09, 143.75, 140.84, 139.33, 137.39, 134.61, 134.06, 131.62, 129.43, 128.61, 128.59, 128.25, 125.08, 123.59, 123.04, 121.63, 111.63, 110.94, 65.70, 49.23, 46.48, 46.31; **ESI-HRMS (*m/z*):** chemical formula: $C_{28}H_{28}ClN_5O_3S_2$, calcd $[M + H]^+$: 582.14003, found $[M + H]^+$: 582.13913; **HPLC-PDA:** λ 300 nm, MeCN:MeOH (1,1), Rt: 4.25 min, 99.64 %.

(E)-N-(4-methylbenzyl)-2-((1-(4-(morpholinosulfonyl)benzyl)-1*H*-indol-3-yl)methylene)hydrazinecarbothioamide **(6d)**

Color: white; **Yield:** 91 %; **M.P.:** 221–223 °C; **FT-IR (cm^{-1}):** 3342, 3145, 3057, 3006, 2968, 1609, 1541, 1462, 1430, 1391, 1298, 1111, 1094, 1052, 968, 806, 737, 670, 559; **^{1}H NMR (600 MHz, DMSO-d_6) δ** 11.35 (1H, s), 8.44–8.33 (2H, m), 8.26 (1H, d, J = 7.9 Hz), 8.05 (1H, s), 7.70 (2H, d, J = 8.1Hz), 7.49 (1 H, d, J = 8.2Hz), 7.45 (2H, d, J = 8.1Hz), 7.27 (2 H, d, J = 7.7 Hz), 7.25–7.19 (1 H, m), 7.15 (3H, d, J = 7.6 Hz), 5.61 (2H, s), 4.86 (2H, d, J = 6.1 Hz), 3.60 (4H, t, J = 4.6 Hz), 2.81 (4H, t, J = 4.6 Hz), 2.28 (3H, s); **^{13}C NMR (150 MHz, DMSO-d_6) δ** 176.95, 143.73, 140.57, 137.39, 137.05, 136.23, 134.50, 134.06, 129.24, 129.23, 128.61, 128.24, 127.57, 125.09, 123.58, 122.89, 121.61, 111.66, 110.96, 65.70, 49.24, 46.89, 46.31, 21.17; **ESI-HRMS (*m/z*):** chemical formula: $C_{29}H_{31}N_5O_3S_2$, calcd $[M + H]^+$: 562.19466, found $[M + H]^+$: 562.19348; **HPLC-PDA:** λ 300 nm, MeCN:MeOH (1,1), Rt: 4.19 min, 99.22 %.

(E)-2-((1-(4-(morpholinosulfonyl)benzyl)-1*H*-indol-3-yl)methylene)-N-(3-nitrophenyl)hydrazinecarbothioamide **(6e)**

Color: off-white; **Yield:** 93 %; **M.P.:** 220–222 °C; **FT-IR (cm^{-1}):** 3308, 3266, 3109, 2960, 2845, 1604, 1527, 1492, 1437, 1408, 1344, 1293, 1262, 1216, 1090, 957, 937, 847, 815, 732, 698, 560; **^{1}H NMR (600 MHz, DMSO-d_6) δ** 11.88 (1H, s), 10.00 (1H, s), 8.74 (1H, t, J = 2.2 Hz), 8.47 (1H, s), 8.34 (1H, d, J = 7.7 Hz), 8.16 (1H, s), 8.12–8.08 (1H, m), 8.04 (1H, ddd, J = 8.3, 2.3, 1.0 Hz), 7.75–7.69 (2H, m), 7.66 (1H, t, J = 8.1Hz), 7.52 (1 H, d, J = 8.3 Hz), 7.47 (2H, dd, J = 8.3, 3.9 Hz), 7.28–7.19 (2H, m), 5.65 (2H, s), 3.60 (5H, t, J = 4.7 Hz), 2.82 (5H, dd, J = 5.8, 3.5 Hz); **^{13}C NMR (150 MHz, DMSO-d_6) δ** 175.04, 147.78, 143.68, 141.98, 141.15, 137.43, 135.07, 134.10, 132.07, 129.71, 128.64, 128.28, 128.26, 125.21, 123.69, 122.98, 121.78, 119.81, 111.43, 111.03, 65.70, 49.31, 46.32; **ESI-HRMS (*m/z*):** chemical formula: $C_{27}H_{26}N_6O_5S_2$, calcd $[M + H]^+$: 579.14844, found $[M + H]^+$: 579.14726; **HPLC-PDA:** λ 300 nm, MeCN:MeOH (1:1), Rt: 4.09 min, 98.24 %.

(E)-2-((1-(4-(morpholinosulfonyl)benzyl)-1*H*-indol-3-yl)methylene)-N-(4-nitrophenyl)hydrazinecarbothioamide **(6f)**

Color: bright yellow; **Yield:** 91 %; **M.P.:** 249–251 °C; **FT-IR (cm^{-1}):** 3293, 3214, 3055, 2987, 1596, 1555, 1498, 1390, 1280, 1193, 1068, 1014, 977, 940, 813, 765, 634, 561; **^{1}H NMR (600 MHz, DMSO-d_6) δ** 12.01 (1H, s), 10.11 (1H, s), 8.48 (1H, s), 8.26 (3H, t, J = 7.0 Hz), 8.17 (1H, s), 8.11 (2H, d, J = 8.6 Hz), 7.72 (2H, d, J = 7.9 Hz), 7.24 (2H, dd, J = 12.9, 7.7 Hz), 5.65 (2H, s), 3.60 (4H, t, J = 4.7 Hz), 2.82 (4H, t, J = 4.6 Hz); **^{13}C NMR (150 MHz, DMSO-d_6) δ** 174.29, 146.24, 143.64, 143.53, 142.16, 137.45, 135.25, 134.11, 128.64, 128.27, 125.21, 124.39, 123.92, 123.73, 122.80, 121.86, 111.36, 111.11, 65.70, 49.33, 46.32; **ESI-HRMS (*m/z*):** chemical formula: $C_{27}H_{26}N_6O_5S_2$, calcd $[M-H]^+$: 577.13279, found $[M-H]^+$: 577.13398; **HPLC-PDA:** λ 300 nm, MeCN:MeOH (1:1), Rt: 3.82 min, 99.25 %.

(E)-N-(4-methoxyphenyl)-2-((1-(4-(morpholinosulfonyl)benzyl)-1*H*-indol-3-yl)methylene)hydrazinecarbothioamide **(6g)**

Color: white; **Yield:** 92 %; **M.P.:** 233–235 °C; **FT-IR (cm^{-1}):** 3310, 3214, 3008, 2967, 2892, 1601, 1570, 1533, 1508, 1458, 1411, 1349, 1298, 1163, 1064, 1014, 941, 793, 558, 528; **^{1}H NMR (600 MHz, DMSO-d_6) δ** 11.54 (1H, s), 9.52 (1H, s), 8.43 (1H, s), 8.31 (1H, d, J = 7.8 Hz), 8.12 (1H, s), 7.77–7.68 (2H, m), 7.51 (1H, d, J = 8.1 Hz), 7.49–7.44 (4H, m), 7.24 (1H, ddd, J = 8.2, 7.0, 1.3 Hz), 7.20 (1H, td, J =

7.5, 7.0, 1.1 Hz), 7.01–6.89 (2H, m), 5.63 (2H, s), 3.78 (3H, s), 3.60 (4H, t, J = 4.7 Hz), 2.87–2.78 (4H, m); **^{13}C NMR (150 MHz, DMSO-d_6) δ** 175.63, 157.33, 143.72, 140.80, 137.39, 134.60, 134.08, 132.69, 128.63, 128.26, 127.74, 125.21, 123.60, 122.87, 121.70, 113.80, 111.60, 110.98, 65.70, 55.74, 49.28, 46.32; **ESI-HRMS (m/z):** chemical formula: $C_{28}H_{29}N_5O_4S_2$, calcd $[M + H]^+$: 564.17392, found $[M + H]^+$: 564.17288; **HPLC-PDA:** λ 300 nm, MeCN:MeOH (1:1), Rt: 3.92 min, 100 %.

(E)-N-(4-fluorophenyl)-2-((1-(4-(morpholinosulfonyl)benzyl)-1*H*-indol-3-yl)methylene)hydrazinecarbothioamide **(6h)**

Color: white; **Yield:** 97 %; **M.P.:** 229–231 °C; **FT-IR (cm^{-1}):** 3327, 3253, 3053, 2912, 1606, 1552, 1501, 1461, 1409, 1388, 1260, 1166, 1069, 975, 815, 672, 560; **^{1}H NMR (600 MHz, DMSO-d_6) δ** 11.64 (1H, s), 9.64 (1H, s), 8.44 (1H, s), 8.33 (1H, d, J = 7.8 Hz), 8.13 (1H, s), 7.71 (2H, d, J = 7.8 Hz), 7.66–7.55 (2H, m), 7.49 (3H, dd, J = 28.1, 8.0 Hz), 7.22 (4H, dq, J = 15.3, 7.1 Hz), 5.64 (2H, s), 3.66–3.54 (4H, m), 2.90–2.76 (4H, m); **^{13}C NMR (150 MHz, DMSO-d_6) δ** 175.56, 160.83, 159.22, 143.71, 141.18, 137.40, 136.18, 134.77, 134.08, 128.63, 128.30, 128.26, 125.20, 123.63, 122.95, 121.72, 115.26, 115.11, 111.54, 110.98, 65.70, 49.29, 46.32; **ESI-HRMS (m/z):** chemical formula: $C_{27}H_{26}FN_5O_3S_2$, calcd $[M + H]^+$: 552.15394, found $[M + H]^+$: 552.15294; **HPLC-PDA:** λ 300 nm, MeCN:MeOH (1:1), Rt: 3.82 min, 99.17 %.

(E)-N-(2,6-dimethylphenyl)-2-((1-(4-(morpholinosulfonyl)benzyl)-1*H*-indol-3-yl)methylene)hydrazinecarbothioamide **(6i)**

Color: white; **Yield:** 94 %; **M.P.:** 201–203 °C; **FT-IR (cm^{-1}):** 3283, 3118, 3034, 2963, 1603, 1534, 1497, 1406, 1392, 1342, 1240, 1111, 1065, 938, 728, 564; **^{1}H NMR (600 MHz, DMSO-d_6) δ** 11.47 (1H, s), 9.30 (1H, s), 8.45 (1H, d, J = 8.0 Hz), 8.43 (1H, s), 8.09 (1H, s), 7.71 (2H, d, J = 8.1 Hz), 7.47 (3H, dd, J = 17.3, 8.1Hz), 7.23 (1 H, t, J = 7.6 Hz), 7.18–7.09 (4H, m), 5.63 (2H, s), 3.60 (4H, t, J = 4.7 Hz), 2.82 (4H, t, J = 4.7 Hz), 2.23 (6H, s); **^{13}C NMR (150 MHz, DMSO-d_6) δ** 176.19, 143.81, 140.71, 138.10, 137.38, 137.16, 134.67, 134.04, 128.60, 128.20, 128.01, 127.26, 125.16, 123.57, 123.46, 121.58, 111.76, 110.80, 65.70, 49.25, 46.32, 18.66; **ESI-HRMS (m/z):** chemical formula: $C_{29}H_{31}N_5O_3S_2$, calcd $[M + H]^+$: 562.19466, found $[M + H]^+$: 562.19343; **HPLC-PDA:** λ 300 nm, MeCN:MeOH (1:1), Rt: 4.12 min, 99.80 %.

(E)-N-(2,3-dichlorophenyl)-2-((1-(4-(morpholinosulfonyl)benzyl)-1*H*-indol-3-yl)methylene)hydrazinecarbothioamide **(6j)**

Color: white; **Yield:** 89 %; **M.P.:** 220–222 °C; **FT-IR (cm^{-1}):** 3249, 2963, 2875, 1610, 1575,ü 1533, 1446, 1410,c1383, 1341, 1298, 1220, 1258, 160, 1065, 1014, 939, 781668, 562; **^{1}H NMR (600 MHz, DMSO-d_6) δ** 11.94 (1H, s), 9.76 (1H, s), 8.53–8.34 (2H, m), 8.23–8.04 (2H, m), 7.71 (2H, d, J = 8.0 Hz), 7.48 (5H, tt, J = 34.1, 7.9 Hz), 7.33–7.12 (2H, m), 5.65 (2H, s), 3.66–3.56 (4H, m), 2.86–2.78 (4H, m); **^{13}C NMR (150 MHz, DMSO-d_6) δ** 174.93, 143.66, 143.64, 141.94, 138.92, 137.48, 135.57, 134.10, 131.98, 128.63, 128.28, 127.95, 127.81, 127.73, 127.27, 125.01, 123.77, 122.95, 121.77, 111.36, 111.13, 65.70, 49.31, 46.32; **ESI-HRMS (m/z):** chemical formula: $C_{27}H^{35}_{25}Cl^{35}ClN_5O_3S_2$, calcd $[M\text{-}H]^+$: 600.06976, found $[M\text{-}H]^+$: 600.07095, chemical formula: $C_{27}H^{35}_{25}Cl^{37}ClN_5O_3S_2$, calcd $[M\text{-}H]^+$: 602.06380, found $[M\text{-}H]^+$: 602.06789, chemical formula: $C_{27}H^{35}_{25}Cl^{35}ClN_5O_3S_2$, calcd $[M + H]^+$: 602.08541, found $[M + H]^+$: 602.08431, chemical formula: $C_{27}H^{35}_{25}Cl^{37}ClN_5O_3S_2$, calcd $[M + H]^+$: 604.07950, found $[M + H]^+$: 604.08139, chemical formula: $C_{27}H^{37}_{25}Cl^{37}ClN_5O_3S_2$, calcd $[M + H]^+$: 606.07530, found $[M + H]^+$: 606.07898; **HPLC-PDA:** λ 254 nm, MeCN:MeOH (1:1), Rt: 4.75 min, 95.33 %.

(E)-N-methyl-2-((1-(4-(pyrrolidin-1-ylsulfonyl)benzyl)-1*H*-indol-3-yl)methylene)hydrazinecarbothioamide **(7a)**

Color: off-white; **Yield:** 93 %; **M.P.:** 235–237 °C; **^{1}H NMR (600 MHz, DMSO-d_6) δ** 11.21 (1H, s), 8.36–8.31 (2H, m), 8.02 (1H, s), 7.95 (1H, q, J = 4.6 Hz), 7.80–7.73 (2H, m), 7.48 (1H, d, J = 8.1 Hz), 7.43 (2H, d, J = 8.1 Hz), 7.26–7.15 (2H, m), 5.59 (2H, s), 3.13–3.06 (7H, m), 1.64–1.55 (4H, m); **^{13}C NMR (150 MHz, DMSO-d_6) δ** 177.31, 143.16, 140.24, 137.35, 135.98, 134.36, 128.26, 128.22, 125.07, 123.53, 123.17, 121.57, 111.70, 110.89, 49.25, 48.22, 31.54, 25.15.

(E)-N-cyclohexyl-2-((1-(4-(pyrrolidin-1-ylsulfonyl)benzyl)-1*H*-indol-3-yl)methylene)hydrazinecarbothioamide **(7b)**

Color: off-white; **Yield:** 97 %; **M.P.:** 257–259 °C; **FT-IR (cm^{-1}):** 3348, 3141, 2978, 2846, 1612, 1537, 1506, 1409, 1331, 1297, 1220, 1152, 1090, 1011, 939, 851, 783, 740, 592, 561; **^{1}H NMR (600 MHz, DMSO-d_6) δ** 11.29 (1H, s), 8.34 (1H, s), 8.07 (2H, d, J = 7.9 Hz), 7.77 (2H, d, J = 8.0 Hz), 7.52 (2H, t, J = 8.8 Hz), 7.43 (2H, d, J = 8.0 Hz), 7.23 (2H, p, J = 7.0 Hz), 5.60 (2H, s), 4.19 (1H, dq, J = 9.8, 5.6, 5.0 Hz), 3.10 (4H, d, J = 6.6 Hz), 1.99–1.87 (2H, m), 1.71 (2H, dq, J = 12.4, 4.1 Hz), 1.66–1.52 (5H, m), 1.53–1.32 (5H, m), 1.27 (1H, t, J = 11.7 Hz); **^{13}C NMR (150 MHz, DMSO-d_6) δ** 175.36, 143.13, 140.09, 137.39, 135.99, 134.36, 128.22, 125.15, 123.56, 122.04, 121.74, 111.54, 111.25, 52.12, 49.27, 48.22, 32.42, 25.57, 25.15, 24.89; **ESI-HRMS (m/z):** chemical formula: $C_{27}H_{33}N_5O_2S_2$, calcd $[M + H]^+$: 524.21539, found $[M + H]^+$: 524.21444; **HPLC-PDA:** λ 300 nm, MeCN:MeOH (1:1), Rt: 4.62 min, 98.50 %.

(E)-N-(4-chlorobenzyl)-2-((1-(4-(pyrrolidin-1-ylsulfonyl)benzyl)-1*H*-indol-3-yl)methylene)hydrazinecarbothioamide **(7c)**

Color: white; **Yield:** 95 %; **M.P.:** 227–229 °C; **FT-IR (cm^{-1}):** 3347, 3155, 3004, 2867, 1611, 1545, 1520, 1489, 1463, 1391, 1328, 1212, 1175, 1153, 1054, 968, 810, 783, 678, 635, 566; **^{1}H NMR (600 MHz, DMSO-d_6) δ** 11.39 (1H, s), 8.52 (1H, t, J = 6.2), 8.37 (1H, s), 8.30 (1H, dt, J = 7.9, 1.0 Hz), 8.05 (1H, s), 7.80–7.72 (2H, m), 7.50–7.47 (1H, m), 7.43 (2H, d, J = 8.2 Hz), 7.40 (4H, s), 7.23 (1H, ddd, J = 8.2, 7.0, 1.2 Hz), 7.17 (1H, ddd, J = 8.0, 7.1, 1.0 Hz), 5.60 (2H, s), 4.90 (2H, d, J = 6.2 Hz), 3.10 (4H, td, J = 6.8, 5.5, 2.8 Hz), 1.69–1.54 (4H, m); **^{13}C NMR (150 MHz, DMSO-d_6) δ** 177.10, 143.14, 140.84, 139.33, 137.37, 135.98, 134.59, 131.63, 129.43, 128.59, 128.23, 125.08, 123.56, 123.04, 121.62, 111.60, 110.95, 49.26, 48.22, 46.49, 25.15; **ESI-HRMS (m/z):** chemical formula: $C_{28}H^{35}_{28}ClN_5O_2S_2$, calcd $[M + H]^+$: 566.14512, found $[M + H]^+$: 566.14412, chemical formula: $C_{28}H^{37}_{28}ClN_5O_2S_2$, calcd $[M + H]^+$: 568.14550, found $[M + H]^+$: 568.14154; **HPLC-PDA:** λ 300 nm, MeCN:MeOH (1:1), Rt: 4.39 min, 99.97 %.

(E)-N-(4-methylbenzyl)-2-((1-(4-(pyrrolidin-1-ylsulfonyl)benzyl)-1*H*-indol-3-yl)methylene)hydrazinecarbothioamide **(7d)**

Color: off-white; **Yield:** 91 %; **M.P.:** 191–193 °C; **FT-IR (cm^{-1}):** 3378, 3138, 3052, 2978, 2872, 1606, 1536, 1462, 1427, 1390, 1214, 1154, 1055, 1008, 933, 788, 705, 681, 590, 558; **^{1}H NMR (600 MHz, DMSO-d_6) δ** 11.35 (1H, s), 8.38 (2H, d, J = 11.8 Hz), 8.25 (1H, d, J = 8.0 Hz), 8.04 (1H, s), 7.77 (2H, d, J = 7.9 Hz), 7.45 (3H, dd, J = 33.9, 8.1Hz), 7.28 (1 H, s), 7.18 (4H, dd, J = 38.4, 7.7 Hz), 5.59 (2H, s), 4.87 (2H, d, J = 6.1 Hz), 3.10 (4H, d, J = 6.1 Hz), 2.28 (3H, s), 1.60 (4H, q, J = 5.4, 4.1 Hz); **^{13}C NMR (150 MHz, DMSO-d_6) δ** 176.95, 143.15, 140.57, 137.36, 137.05, 136.23, 135.98, 134.49, 129.24, 128.23, 127.56, 125.09, 123.55, 122.89, 121.59, 111.62, 110.98, 49.26, 48.22, 46.89, 25.15, 21.17; **ESI-HRMS (m/z):** chemical formula: $C_{29}H_{31}N_5O_2S_2$, calcd $[M + H]^+$: 546.19974, found $[M + H]^+$: 546.19818; **HPLC-PDA:** λ 300 nm, MeCN:MeOH (1:1), Rt: 4.30 min, 99.77 %.

(E)-N-(3-nitrophenyl)-2-((1-(4-(pyrrolidin-1-ylsulfonyl)benzyl)-1*H*-indol-3-yl)methylene)hydrazinecarbothioamide **(7e)**

Color: bright yellow; **Yield:** 98 %; **M.P.:** 163–165 °C; **FT-IR (cm^{-1}):** 3275, 3095, 2981, 2875, 1612, 1593, 1546, 1523, 1463, 1435, 1411, 1387, 1297, 1161, 1093, 1006, 940, 885, 799, 700, 638, 559; **^{1}H NMR (600 MHz, DMSO-d_6) δ** 11.88 (1H, s), 10.00 (1H, s), 8.74 (1H, t, J = 2.2 Hz), 8.47 (1H, s), 8.34 (1H, dd, J = 7.4, 1.5 Hz), 8.15 (1H, s), 8.09 (1H, ddd, J = 8.2, 2.1, 1.0 Hz), 8.04 (1H, ddd, J = 8.2, 2.3, 1.0 Hz), 7.81–7.75 (2H, m), 7.66 (1H, t, J = 8.1Hz), 7.54–7.47 (1 H, m), 7.44 (2H, d, J = 8.2Hz), 7.29–7.16 (2H, m), 5.63 (2 H, s), 3.17–3.04 (4H, m), 1.66–1.54 (4H, m); **^{13}C NMR (150 MHz, DMSO-d_6) δ** 175.03, 147.77, 143.09, 141.98, 141.15, 137.40, 136.02, 135.06, 132.07, 129.71, 128.24, 125.22, 123.65, 122.97, 121.77, 119.81, 111.39, 111.05, 49.34, 48.23, 25.16; **ESI-HRMS (m/z):** chemical formula: $C_{27}H_{26}N_6O_4S_2$, calcd $[M + H]^+$: 563.15352, found $[M + H]^+$: 563.15236, chemical formula:

$C_{27}H_{26}N_6O_4S_2$, calcd $[M-H]^+$: 561.13787, found $[M-H]^+$: 561.13872; **HPLC-PDA:** λ 300 nm, MeCN:MeOH (1:1), Rt: 4.12 min, 99.88 %.

(E)-N-(4-nitrophenyl)-2-((1-(4-(pyrrolidin-1-ylsulfonyl)benzyl)-1*H*-indol-3-yl)methylene)hydrazinecarbothioamide **(7f)**

Color: bright yellow; **Yield:** 92 %; **M.P.:** 240–242 °C; **FT-IR (cm^{-1}):** 3274, 3143, 2972, 2873, 1695, 1558, 1495, 1457, 1410, 1329, 1270, 1159, 1111, 1043, 1092, 1008, 846, 751, 700, 588, 538; **^{1}H NMR (600 MHz, DMSO-d_6)** δ 12.00 (1H, s), 10.11 (1H, s), 8.48 (1H, s), 8.26 (3H, dd, J = 9.5, 2.5 Hz), 8.17 (1H, s), 8.11 (2H, d, J = 9.0 Hz), 7.81–7.76 (2H, m), 7.51 (1H, d, J = 8.2Hz), 7.44 (2H, d, J = 8.1 Hz), 7.23 (2H, ddd, J = 10.6, 7.6, 1.4 Hz), 5.63 (2 H, s), 3.15–3.05 (5H, m), 1.67–1.55 (5H, m); **^{13}C NMR (150 MHz, DMSO-d_6)** δ 185.31, 174.28, 146.24, 143.52, 143.06, 142.16, 137.43, 136.03, 135.26, 128.42, 128.29, 128.24, 125.21, 124.39, 123.92, 123.69, 122.80, 121.85, 111.31, 111.13, 49.34, 48.23, 25.16; **ESI-HRMS (m/z):** chemical formula: $C_{27}H_{26}N_6O_4S_2$, calcd $[M-H]^+$: 561.13787, found $[M-H]^+$: 561.13905; **HPLC-PDA:** λ 300 nm, MeCN:MeOH (1:1), Rt: 4.30 min, 98.77 %.

(E)-N-(4-methoxyphenyl)-2-((1-(4-(pyrrolidin-1-ylsulfonyl)benzyl)-1*H*-indol-3-yl)methylene)hydrazinecarbothioamide **(7g)**

Color: off-white; **Yield:** 90 %; **M.P.:** 232–234 °C; **FT-IR (cm^{-1}):** 3331, 3124, 3057, 2974, 2884, 1605, 1539, 1495, 1462, 1372, 1333, 1275, 1169, 1085, 1054, 1032, 796, 716, 641, 596; **^{1}H NMR (600 MHz, DMSO-d_6)** δ 11.54 (1H, s), 9.52 (1H, s), 8.43 (1H, s), 8.31 (1H, d, J = 7.8 Hz), 8.11 (1H, s), 7.82–7.70 (2H, m), 7.52–7.48 (1H, m), 7.48–7.41 (4H, m), 7.23 (1H, ddd, J = 8.2, 7.1, 1.3 Hz), 7.19 (1H, ddd, J = 8.0, 7.1, 1.1 Hz), 6.99–6.87 (2H, m), 5.61 (2H, s), 3.78 (3H, s), 3.16–3.04 (4H, m), 1.66–1.56 (4H, m); **^{13}C NMR (150 MHz, DMSO-d_6)** δ 175.60, 157.33, 143.13, 140.82, 137.37, 136.00, 134.60, 132.68, 128.24, 127.75, 125.21, 123.56, 122.86, 121.68, 113.80, 111.55, 111.00, 55.74, 49.30, 48.23, 25.15; **ESI-HRMS (m/z):** chemical formula: $C_{28}H_{29}N_5O_3S_2$, calcd $[M + H]^+$: 548.17901, found $[M + H]^+$: 548.17780; **HPLC-PDA:** λ 300 nm, MeCN:MeOH (1:1), Rt: 4.08 min, 99.83 %.

(E)-N-(4-fluorophenyl)-2-((1-(4-(pyrrolidin-1-ylsulfonyl)benzyl)-1*H*-indol-3-yl)methylene)hydrazinecarbothioamide **(7h)**

Color: off-white; **Yield:** 96 %; **M.P.:** 230–232 °C; **FT-IR (cm^{-1}):** 3341, 3120, 3058, 2968, 1602, 1548, 1493, 1408, 1369, 1333, 1307, 1277, 1211, 1150, 1086, 1039, 985, 913, 841, 755, 642, 540; **^{1}H NMR (600 MHz, DMSO-d_6)** δ 11.63 (1H, s), 9.63 (1H, s), 8.43 (1H, s), 8.32 (1H, d, J = 8.0 Hz), 8.12 (1H, s), 7.82–7.73 (2H, m), 7.65–7.57 (2H, m), 7.50 (1H, dd, J = 8.0, 1.1 Hz), 7.48–7.40 (2H, m), 7.27–7.15 (4H, m), 5.61 (2H, s), 3.17–3.07 (4H, m), 1.68–1.57 (4H, m); **^{13}C NMR (150 MHz, DMSO-d_6)** δ 175.56, 160.83, 159.22, 143.12, 141.18, 137.38, 136.19, 136.17, 136.00, 134.76, 128.30, 128.24, 125.20, 123.59, 122.94, 121.70, 115.26, 115.11, 111.49, 111.00, 49.30, 48.23, 25.15; **ESI-HRMS (m/z):** chemical formula: $C_{27}H_{26}FN_5O_2S_2$, calcd $[M + H]^+$: 536.15902, found $[M + H]^+$: 536.15763; **HPLC-PDA:** λ 300 nm, MeCN:MeOH (1:1), Rt: 4.31 min, 98.78 %.

(E)-N-(2,6-dimethylphenyl)-2-((1-(4-(pyrrolidin-1-ylsulfonyl)benzyl)-1*H*-indol-3-yl)methylene)hydrazinecarbothioamide **(7i)**

Color: white; **Yield:** 94 %; **M.P.:** 219–221 °C; **FT-IR (cm^{-1}):** 3605, 3560, 3447, 3340, 3106, 2968, 1607, 1571, 1535, 1498, 1390, 1339, 1270, 1194, 1052, 1008, 952, 819, 633, 588, 541; **^{1}H NMR (600 MHz, DMSO-d_6)** δ 11.47 (1H, s), 9.29 (1H, s), 8.52–8.37 (2H, m), 8.09 (1H, s), 7.77 (2H, d, J = 8.3 Hz), 7.47 (1H, d, J = 8.2Hz), 7.43 (2 H, d, J = 8.1Hz), 7.25–7.19 (1 H, m), 7.18–7.09 (4H, m), 5.61 (2H, s), 3.16–3.05 (4H, m), 2.23 (6H, s), 1.68–1.55 (4H, m); **^{13}C NMR (150 MHz, DMSO-d_6)** δ 176.18, 143.22, 140.70, 138.10, 137.35, 137.16, 135.96, 134.66, 128.21, 128.19, 128.01, 127.26, 125.16, 123.52, 123.46, 121.56, 111.72, 110.82, 49.27, 48.23, 25.15, 18.65; **ESI-HRMS (m/z):** chemical formula: $C_{29}H_{31}N_5O_2S_2$, calcd $[M + H]^+$: 546.19974, found $[M + H]^+$: 546.19837; **HPLC-PDA:** λ 300 nm, MeCN:MeOH (1:1), Rt: 4.18 min, 99.41 %.

(E)-N-(2,3-dichlorophenyl)-2-((1-(4-(pyrrolidin-1-ylsulfonyl)benzyl)-1*H*-indol-3-yl)methylene)hydrazinecarbothioamide **(7j)**

Color: white; **Yield:** 93 %; **M.P.:** 201–203 °C; **FT-IR (cm^{-1}):** 3269, 4157, 3115, 3047, 2974, 1615, 1578, 1539, 1509, 1450, 1388, 1336, 1264, 1195, 1116, 1044, 807, 776, 633, 587, 559; **^{1}H NMR (600 MHz, DMSO-d_6)** δ 11.94 (1H, s), 9.76 (1H, s), 8.46 (1H, s), 8.37 (1H, d, J = 7.9 Hz), 8.14 (1H, s), 8.10 (1H, dd, J = 8.2, 1.5 Hz), 7.78 (2H, d, J = 8.3 Hz), 7.54 (1H, dd, J = 8.1, 1.5 Hz), 7.51 (1H, d, J = 8.2 Hz), 7.47–7.39 (3H, m), 7.25 (1H, ddd, J = 8.3, 7.0, 1.2 Hz), 7.22–7.16 (1H, m), 5.62 (2H, s), 3.15–3.05 (4H, m), 1.65–1.55 (4H, m); **^{13}C NMR (150 MHz, DMSO-d_6)** δ 174.91, 143.05, 141.93, 138.91, 137.45, 136.02, 135.56, 131.98, 128.27, 128.24, 127.95, 127.78, 127.71, 127.23, 125.02, 123.73, 122.93, 121.75, 111.31, 111.15, 49.33, 48.23, 25.15; **ESI-HRMS (m/z):** chemical formula: $C_{27}H_{25}^{35}Cl^{35}ClN_5O_2S_2$, calcd $[M + H]^+$: 586.09050, found $[M + H]^+$: 586.08937, chemical formula: $C_{27}H_{25}^{35}Cl^{37}ClN_5O_2S_2$, calcd $[M + H]^+$: 588.08460, found $[M + H]^+$: 588.08653, chemical formula: $C_{27}H_{25}^{35}Cl^{35}ClN_5O_2S_2$, calcd $[M-H]^+$: 584.07485, found $[M-H]^+$: 584.07631, chemical formula: $C_{27}H_{25}^{35}Cl^{37}ClN_5O_2S_2$, calcd $[M-H]^+$: 586.0689, found $[M-H]^+$: 586.07363; **HPLC-PDA:** λ 300 nm, MeCN:MeOH (1:1), Rt: 5.00 min, 99.90 %.

4.4. Cell culture

In this study, CCD 1079Sk human skin fibroblast cells and SH-SY5Y human neuroblastoma cells were employed to evaluate the in vitro cytotoxic effects of the compounds. Both cell lines were cultured in Dulbecco's Modified Eagle Medium/Nutrient Mixture F-12 (DMEM/F12, Gibco, MD, USA), supplemented with 10 % fetal bovine serum (FBS) and 1 % penicillin-streptomycin (Gibco, MD, USA) to provide essential nutrients and maintain sterility. The cells were maintained in a humidified atmosphere at 37 °C with 5 % CO_2 to closely mimic physiological conditions and support optimal cell growth. Culture medium was refreshed every 48 h, and cells were subcultured at 70–80 % confluency using 0.25 % trypsin-EDTA (Gibco, MD, USA) to detach adherent cells. Before each experimental procedure, cell morphology, viability, and density were monitored using an inverted phase-contrast microscope to ensure consistency across experimental replicates [68].

4.5. MTT assay

Cell viability of SH-SY5Y human neuroblastoma cells and CCD 1079Sk normal human skin fibroblast cells was evaluated using the MTT assay (3-(4,5-dimethylthiazol-2-yl)-2,5-diphenyltetrazolium bromide). A suspension of 10.000 cells per well in 200 µL was seeded into 96-well plates and incubated overnight to allow for cell attachment and initial growth. Following incubation, cells were treated with seven different concentrations (3.125, 6.25, 12.5, 25, 50, and 100 µM) of the target compounds **6(a-j)** and **7(a-j)** along with the reference drug sorafenib, for 24 h. After treatment, MTT solution was added to each well at a final concentration of 0.1 mg/mL, and the plates were incubated for an additional 3 h at 37 °C to allow metabolically active cells to reduce MTT into formazan crystals. The medium containing MTT was then carefully removed, and dimethyl sulfoxide (DMSO) was added to solubilize the formazan. Plates were kept at room temperature in the dark for 30 min to ensure complete dissolution. Absorbance was measured at 570 nm using a microplate reader (BioTek Instruments, Inc., USA). Cell viability was expressed as a percentage relative to untreated control cells. The selectivity index (SI) for each compound was calculated by dividing the IC_{50} value obtained in normal CCD 1079Sk fibroblasts by the IC_{50} value in SH-SY5Y neuroblastoma cells, providing a quantitative measure of cancer selectivity [69–71].

4.6. Cholinesterase activity

Enzyme inhibition was investigated in bioactivity experiments using a slightly modified version of the colorimetric Ellman method (1). The reaction was carried out using butyrylthiocholine iodide (BChI) and acetylthiocholine iodide (AChI) as substrates. 5,5'-Dithio-bis(2-nitro-

benzoic)acid (DTNB) was employed to quantify the activities of AChE and BChE. The enzymes recombinant human AChE and human serum BChE were used in in vitro enzyme activity experiments. The following procedure was used for the activity: 1.0 mL of Tris/HCl buffer (1.0 M, pH 8.0) and 10 mL of sample solution at various concentrations were added to deionized water (2,3). The final solution was then incubated for 10 min at 25 °C after 50 mL of AChE or BChE solution had been combined. 50 mL of DTNB (0.5 mM) was added following incubation. When 50 mL of AChI or BChI was added, the reaction was permitted to be initiated. The creation of the yellow 5-thio-2-nitrobenzoate anion, which is the product of the interaction between DTNB and thiocholine produced by the enzymatic hydrolysis of AChI or BChI, with a maximum absorbance at 412 nm, served as a spectrophotometric indicator of the hydrolysis of these substrates. Plots of activity (%) vs chemicals were used to determine IC50 values. However, the Lineweaver-Burk graph was used to determine Ki values. At least three runs of each experiment were conducted ($N = 3$) (4,5).

4.7. Computational studies

Molecular docking and dynamics simulations were conducted using Schrödinger Molecular Modeling Software (2025–1) with the Maestro interface (version 14.5) and Desmond (D. E. Shaw Research). Protein and ligand preparation followed established protocols from our group [72]. Three-dimensional crystallographic structures of the target enzymes, AChE (PDB ID: 4EY7), BChE (PDB ID: 6ESJ), and YAP–TED1 (PDB ID: 9FZA) were obtained from the Protein Data Bank and optimized using Schrödinger's Protein Preparation Wizard. The chemical structures of the ligands were drawn using ChemDraw and converted to SMILES format, then prepared using Schrödinger's LigPrep module to generate energy-minimized 3D conformers with proper ionization states and tautomers at pH 7.0 ± 2. Glide docking and Induced Fit Docking (IFD) were performed to dock the ligands into the target receptors, generating 20 docking poses per ligand, which were evaluated using Glide XP (extra precision) scoring. The best docking poses were selected based on their IFD docking scores. Prime MM-GBSA analysis, employing the OPLS4e force field and the VSGB solvation model, was used to estimate binding free energies for the protein–ligand complexes. Molecular dynamics (MD) simulations were carried out using Desmond, where each protein–ligand complex was solvated using TIP4P water molecules and neutralized with counter ions (Na^+ and Cl^-), followed by a 250-ns simulation under NPT ensemble conditions (300 K, 1 atm). RMSD values of the protein backbone and ligand atoms were monitored to assess the overall structural stability, while RMSF plots were analyzed to evaluate the flexibility of individual amino acid residues. Hydrogen bonds, hydrophobic contacts, and salt bridges were also examined to understand key stabilizing interactions throughout the simulation [73].

4.8. Statistical analysis

Statistical analyses were applied using the Minitab 13 statistical software package (Minitab Inc. State College, PA, USA). All results are expressed as the means, including their standard error of the mean (SEM). Comparisons between groups were performed using Student's *t*-test, and $P < 0.05$ was selected as the level required for statistical significance.

CRediT authorship contribution statement

Zahra Batool: Writing – original draft, Methodology, Investigation, Formal analysis. **Gülbahar Özge Alim Toraman:** Software, Formal analysis, Data curation. **Furkan Çakır:** Validation, Software, Investigation, Formal analysis. **Gülaçtı Topçu:** Investigation, Formal analysis. **Parham Taslimi:** Writing – original draft, Validation, Formal analysis, Data curation. **Rima D. Alharthy:** Validation, Formal analysis, Resources, Conceptualization, Writing – original draft. **Ajmal Khan:** Software, Investigation. **Ahmed Al-Harrasi:** Resources, Formal analysis. **Zahid Shafiq:** Writing – original draft, Supervision, Conceptualization. **Halil Şenol:** Writing – original draft, Methodology, Investigation, Conceptualization.

Funding declaration

This Project was funded by the Deanship of Scientific Research (DSR) at King Abdulaziz University, Jeddah under grant no. (IPP: 66–665-2025).

Declaration of competing interest

The authors declare that they have no known competing financial interests or personal relationships that could have appeared to influence the work reported in this paper.

Acknowledgement

This Project was funded by the Deanship of Scientific Research (DSR) at King Abdulaziz University, Jeddah under grant no. (IPP: 66-665-2025). The authors, therefore, acknowledge with thanks DSR for technical and financial support.

Appendix A. Supplementary data

Supplementary data to this article can be found online at https://doi.org/10.1016/j.bioorg.2025.109252.

Data availability

No data was used for the research described in the article.

References

[1] B.W. Corn, D.B. Feldman, Cancer statistics, 2025: a hinge moment for optimism to morph into hope? CA Cancer J. Clin. 75 (1) (2025) 7–9.
[2] R.L. Siegel, T.B. Kratzer, A.N. Giaquinto, H. Sung, A. Jemal, Cancer statistics, 2025, CA Cancer J. Clin. 75 (1) (2025) 10–45.
[3] D.M. Hausman, What is cancer?, Perspect, Biol. Med. 62 (4) (2019) 778–784.
[4] N.C. Colon, D.H. Chung, Neuroblastoma, Adv. Pediatr. Infect. Dis. 58 (1) (2011) 297–311.
[5] S. Rajpoot, R. Kumar, R. Singh, S. Chandel, Advancements in neuroblastoma treatment: FDA-approved drugs and role of phytochemicals, Mol. Biol. Rep. 52 (1) (2025).
[6] M.G. Mamatha, M.A. Ansari, M.Y. Begum, B.D. Prasad, A. Al Fatease, U. Hani, M. N. Alomary, S. Sultana, S.M. Punekar, M.B. Nivedika, T.R. Lakshmeesha, T. Ravikiran, Green synthesis of cerium oxide nanoparticles, Characterization, and their Neuroprotective Effect on Hydrogen Peroxide-Induced Oxidative Injury in Human Neuroblastoma (SH-SY5Y), Cell Line, ACS OMEGA vol. 9 (2) (2024) 2639–2649.
[7] R. Manikandan, K. Devi, D. Rajalingam, Synthesis and evaluation of 2, 5-substituted Pyrazolone for neuroprotective potential in SH-SY5Y human neuroblastoma cells, Indian Journal of Pharmaceutical Education and Research 59 (1) (2025) s323–s332.
[8] D. Tzankova, H. Kuteva, E. Mateev, D. Stefanova, A. Dzhemadan, Y. Yordanov, A. Mateeva, V. Tzankova, M. Kondeva-Burdina, A. Zlatkov, M. Georgieva, Synthesis, DFT study, and in vitro evaluation of antioxidant properties and cytotoxic and Cytoprotective effects of new Hydrazones on SH-SY5Y neuroblastoma cell lines, Pharmaceuticals 16 (9) (2023).
[9] M.B. Muluk, S.T. Dhumal, N.N. Rehman, P.P. Dixit, K.R. Kharat, K.P. Haval, Synthesis, anticancer and antimicrobial evaluation of new (E)-N′-Benzylidene-2-(2-ethylpyridin-4-yl)-4-methylthiazole-5-carbohydrazides, ChemistrySelect 4 (31) (2019) 8993–8997.
[10] M.B. Muluk, A.S. Ubale, S.T. Dhumal, N.N. Rehman, P.P. Dixit, K.K. Kharat, P. B. Choudhari, K.P. Haval, Synthesis, anticancer and antimicrobial evaluation of new pyridyl and thiazolyl clubbed hydrazone scaffolds, Synth. Commun. 50 (2) (2020) 243–255.
[11] H. Yang, H. Zhou, M. Fu, H. Xu, H. Huang, M. Zhong, M. Zhang, W. Hua, K. Lv, G. Zhu, TMEM64 aggravates the malignant phenotype of glioma by activating the Wnt/β-catenin signaling pathway, Int. J. Biol. Macromol. 260 (2024) 129332.
[12] X. Wu, M. Fu, C. Ge, H. Zhou, H. Huang, M. Zhong, M. Zhang, H. Xu, G. Zhu, W. Hua, m6A-mediated upregulation of LncRNA CHASERR promotes the progression of glioma by modulating the miR-6893-3p/TRIM14 axis, Mol. Neurobiol. 61 (8) (2024) 5418–5440.

[13] W.-J. Zeng, L. Zhang, H. Cao, D. Li, H. Zhang, Z. Xia, R. Peng, A novel inflammation-related lncRNAs prognostic signature identifies LINC00346 in promoting proliferation, migration, and immune infiltration of glioma, Front. Immunol. 13 (2022) 810572.
[14] G.O. Alim Toraman, S. Atasoy, H. Şenol, E.S. Okudan, H.O. Dinc, G. Topcu, LC-MS and GC-MS Analyses on Green Algae *Penicillus capitatus*: Cytotoxic, Antimicrobial and Anticholinesterase Activity Screening Enhanced by Molecular Docking & Dynamics and ADME Studies, Chem. Biodivers. 21 (10) (2024) e202400915.
[15] F.S. Tokali, P. Taslimi, N. Sadeghian, T. Taskin-Tok, I. Gülçin, Synthesis, characterization, bioactivity impacts of new Anthranilic acid Hydrazones containing aryl sulfonate moiety as Fenamate Isosteres, ChemistrySelect 8 (13) (2023) e202300241.
[16] F.S. Tokalı, P. Taslimi, B. Tüzün, A. Karakuş, N. Sadeghian, İ. Gülçin, Synthesis of new carboxylates and sulfonates containing thiazolidin-4-one ring and evaluation of inhibitory properties against some metabolic enzymes, J. Iran. Chem. Soc. 20 (10) (2023) 2631–2642.
[17] F.S. Tokali, P. Taslimi, B. Tuzun, A. Karakus, N. Sadeghian, I. Gulcin, Novel Quinazolinone derivatives: potential synthetic analogs for the treatment of Glaucoma, Alzheimer's disease and diabetes mellitus, Chem. Biodivers. 20 (10) (2023) e202301134.
[18] G. Topcu, A. Akdemir, U. Kolak, M. Ozturk, M. Boga, F. Bahadori, S.D.H. Cakmar, Anticholinesterase and antioxidant activities of natural Abietane Diterpenoids with molecular docking studies, Curr. Alzheimer Res. 17 (3) (2020) 269–284.
[19] C. Bayrak, P. Taslimi, N. Kilinc, I. Gulcin, A. Menzek, Synthesis and biological activity of some bromophenols and their derivatives including natural products, Chem. Biodivers. 20 (8) (2023) e202300469.
[20] B. Culhaoglu, A. Capan, M. Boga, M. Ozturk, T. Ozturk, G. Topcu, Antioxidant and anticholinesterase activities of some Dialkylamino substituted 3-Hydroxyflavone derivatives, Med. Chem. 13 (3) (2017) 254–259.
[21] I. Gulcin, O.V. Petrova, P. Taslimi, S.F. Malysheva, E.Y. Schmidt, L.N. Sobenina, N. K. Gusarova, B.A. Trofimov, B. Tuzun, V.M. Farzaliyev, S. Alwasel, A.R. Sujayev, Synthesis, characterization, molecular docking, acetylcholinesterase and α-glycosidase inhibition profiles of nitrogen-based novel heterocyclic compounds, ChemistrySelect 7 (19) (2022) e202200370.
[22] I. Gulcin, A. Scozzafava, C.T. Supuran, H. Akincioglu, Z. Koksal, F. Turkan, S. Alwasel, The effect of caffeic acid phenethyl ester (CAPE) on metabolic enzymes including acetylcholinesterase, butyrylcholinesterase, glutathione S-transferase, lactoperoxidase, and carbonic anhydrase isoenzymes I, II, IX, and XII, J. Enzym. Inhib. Med. Chem. 31 (6) (2016) 1095–1101.
[23] I. Gulcin, B. Trofimov, R. Kaya, P. Taslimi, L. Sobenina, E. Schmidt, O. Petrova, S. Malysheva, N. Gusarova, V. Farzaliyev, A. Sujayev, S. Alwasel, C.T. Supuran, Synthesis of nitrogen, phosphorus, selenium and sulfur-containing heterocyclic compounds - determination of their carbonic anhydrase, acetylcholinesterase, butyrylcholinesterase and alpha-glycosidase inhibition properties, Bioorg. Chem. 103 (2020) 104171.
[24] P. Taslimi, H. Akincioglu, I. Gulcin, Synephrine and phenylephrine act as alpha-amylase, alpha-glycosidase, acetylcholinesterase, butyrylcholinesterase, and carbonic anhydrase enzymes inhibitors, J. Biochem. Mol. Toxicol. 31 (11) (2017).
[25] P. Taslimi, M. Işık, F. Türkan, M. Durgun, C. Türkeş, İ. Gülçin, Ş. Beydemir, Benzenesulfonamide derivatives as potent acetylcholinesterase, α-glycosidase, and glutathione S-transferase inhibitors: biological evaluation and molecular docking studies, J. Biomol. Struct. Dyn. 39 (15) (2021) 5449–5460.
[26] S. Roytrakul, J. Jaresitthikunchai, N. Phaonakrop, S. Charoenlappanit, S. Thaisakun, N. Kumsri, T. Arpornsuwan, Secretomic changes of amyloid beta peptides on Alzheimer's disease related proteins in differentiated human SH-SY5Y neuroblastoma cells, Peerj 12 (2024).
[27] D. Vicente-Zurdo, B. Gómez-Gómez, I. Romero-Sánchez, N. Rosales-Conrado, M. E. León-González, Y. Madrid, Cytotoxicity, uptake and accumulation of selenium nanoparticles and other selenium species in neuroblastoma cell lines related to Alzheimer's disease by using cytotoxicity assays, TEM and single cell-ICP-MS, Anal. Chim. Acta 1249 (2023).
[28] M.E. Arslan, H. Turkez, A. Mardinoglu, In vitro neuroprotective effects of farnesene sesquiterpene on alzheimer's disease model of differentiated neuroblastoma cell line, Int. J. Neurosci. 131 (8) (2021) 745–754.
[29] L. Tang, Q. Xiang, J. Xiang, Y. Zhang, J. Li, Tripterygium glycoside ameliorates neuroinflammation in a mouse model of Aβ25-35-induced Alzheimer's disease by inhibiting the phosphorylation of IκBα and p38, Bioengineered 12 (1) (2021) 8540–8554.
[30] M. Islam, S. Ullah, A. Khan, Z. Batool, S.N. Mali, S.S. Gurav, K.A. Dahlous, S. Mohammad, J. Hussain, A. Al-Harrasi, Design, synthesis, in vitro, and in silico studies of 4-fluorocinnamaldehyde based thiosemicarbazones as urease inhibitors, Sci. Rep. 15 (1) (2025) 609.
[31] Z. Batool, S.M. Dutt, M. Al-Rashida, N.E. Gelsleichter, J. Pelletier, J. Sévigny, T. Islam, H. Aftab, T.M. Almutairi, F. Çakır, N-hexylsulfonyl indole based thiosemicarbazones as potent and selective ecto-5′-nucleotidase and NTPDase inhibitors, Bioorg. Chem. 163 (2025) 108717.
[32] A.D. Badar, S.M. Sulakhe, M.B. Muluk, N.N. Rehman, P.P. Dixit, P.B. Choudhari, G. M. Bondle, K.P. Haval, Synthesis, antimicrobial evaluation and docking study of novel thiosemicarbazone clubbed with 1, 2, 3-triazoles, Curr. Bioact. Compd. 17 (6) (2021) 12–21.
[33] H. Abdelbaki, A. Djemoui, M.R. Ouahrani, M. Messaoudi, I. Ben Amor, H. Alsaeedi, D. Cornu, M. Bechelany, A. Barhoum, Synthesis of bioactive 1,4-disubstituted 1,2,3-triazole-linked Thiosemicarbazone derivatives using Cu2O microbeads catalysis for enhanced antibacterial and antioxidant activities, J. Mol. Struct. 1324 (2025).
[34] G.L.S. Sousa, N.F. Nadur, L.D.P. Ferreira, T.D. Honório, A. Simon, L.M. Cabral, M.L. M. Santos, B. Andrade, E.V. de Lima, J.R. Clarke, R.N. Castro, R.O.D. Moura, A. E. Kümmerle, Discovery of novel thiosemicarbazone-acridine targeting butyrylcholinesterase with antioxidant, metal complexing and neuroprotector abilities as potential treatment of Alzheimer's disease: in vitro, in vivo, and in silico studies, Eur. J. Med. Chem. 281 (2025).
[35] A. Paneth, B. Kaproń, T. Plech, R. Paduch, N. Trotsko, P. Paneth, Combined in silico and in vitro analyses to assess the anticancer potential of thiazolidinedione-Thiosemicarbazone hybrid molecules, Int. J. Mol. Sci. 24 (24) (2023).
[36] E.P. Mendes, C.M. Goulart, O.A. Chaves, V.D.S. Faiões, M.M. Canto-Carvalho, G. C. Machado, E.C. Torres-Santos, A. Echevarria, Evaluation of Novel Chalcone-Thiosemicarbazones Derivatives as Potential Anti-Leishmania Amazonensis Agents and its HSA Binding Studies, Biomolecules 9 (11) (2019) 643.
[37] A. Saeed, N.A. Al-Masoudi, M. Latif, Synthesis and antiviral activity of new substituted methyl [2-(arylmethylene-hydrazino)-4-oxo-thiazolidin-5-ylidene] acetates, Arch Pharm (Weinheim) 346 (8) (2013) 618–625.
[38] A. Rasool, Z. Batool, M. Khan, S.A. Halim, Z. Shafiq, A. Temirak, M.A. Salem, T. E. Ali, A. Khan, A. Al-Harrasi, Bis-pharmacophore of cinnamaldehyde-clubbed thiosemicarbazones as potent carbonic anhydrase-II inhibitors, Sci. Rep. 12 (1) (2022) 16095.
[39] M.B. Muluk, S.T. Dhumal, N.N.M.A. Rehman, P.P. Dixit, K.R. Kharat, K.P. Haval, Synthesis, anticancer and antimicrobial evaluation of new (E)-N′-Benzylidene-2-(2-ethylpyridin-4-yl)-4-methylthiazole-5-carbohydrazides, ChemistrySelect 4 (31) (2019) 8993–8997.
[40] D. Zolotareva, A. Zazybin, A. Dauletbakov, Y. Belyankova, B.G. Parache, S. Tursynbek, T. Seilkhanov, A. Kairullinova, Morpholine, Piperazine, and Piperidine derivatives as antidiabetic agents, Molecules 29 (13) (2024).
[41] I. Mushtaq, A. Ahmed, Synthesis of biologically active sulfonamide-based indole analogs: a review, Future Journal of Pharmaceutical Sciences 9 (1) (2023).
[42] S. Kumar, P. Bishnoi, N. Chauhan, P. Kumar, R. Aggarwal, Therapeutic potential of morpholine-based compounds in neurodegenerative diseases: SAR insights and analysis, Future Med. Chem. 17 (12) (2025) 1439–1455.
[43] B.H. Ganesh, A.G. Raj, B. Aruchamy, P. Nanjan, C. Drago, P. Ramani, Pyrrole: a decisive scaffold for the development of therapeutic agents and structure-activity relationship, ChemMedChem 19 (1) (2024) e202300447.
[44] S. Tariq, F. Rahim, H. Ullah, M. Sarfraz, R. Hussain, S. Khan, M.U. Khan, W. Rehman, A. Hussain, M.A. Bhat, M.K. Farooqi, S.A.A. Shah, N. Iqbal, Synthesis, in vitro biological evaluation and molecular modeling of Benzimidazole-based pyrrole/Piperidine hybrids derivatives as potential anti-Alzheimer agents, Pharmaceuticals 17 (4) (2024).
[45] O.G.V. Petrova, D.N. Tomilin, H. Şenol, K.V. Belyaeva, L.P. Nikitina, L.A. Oparina, L.N. Sobenina, B.A. Trofimov, N. Sadeghian, P. Taslimi, V. Farzaliyev, A. Sujayev, İ. Gulçin, Synthesis of pyrrole-heterocyclic derivatives as anti-Alzheimer and antidiabetic candidates: an in vitro-in silico study, J. Mol. Struct. 1315 (2024) 138998.
[46] Z. Batool, S. Ullah, A. Khan, S.N. Mali, S.S. Gurav, R.D. Jawarkar, A. Alshammari, N.A. Albekairi, A. Al-Harrasi, Z. Shafiq, Design, synthesis, QSAR modelling and molecular dynamic simulations of N-tosyl-indole hybrid thiosemicarbazones as competitive tyrosinase inhibitors, Sci. Rep. 14 (1) (2024) 25754.
[47] Z. Batool, S. Ullah, A. Khan, F. Siddique, S. Nadeem, A. Alshammari, N. A. Albekairi, R. Talib, A. Al-Harrasi, Z. Shafiq, Design, synthesis, and in vitro and in silico study of 1-benzyl-indole hybrid thiosemicarbazones as competitive tyrosinase inhibitors, RSC Adv. 14 (39) (2024) 28524–28542.
[48] B. Zengin Kurt, M. Gökçe, H. Şenol, D. Öztürk Civelek, G. Dandin, I. Gazioglu, Synthesis, cytotoxic evaluation, and in silico studies of novel benzenesulfonamide-thiazolidinone derivatives against colorectal carcinoma, J. Mol. Struct. 1321 (2025) 140153.
[49] A. Behcet, P. Taslimi, B. Sen, T. Taskin-Tok, A. Aktas, Y. Gok, M. Aygun, I. Gulcin, New palladium complexes with N-heterocyclic carbene and morpholine ligands: synthesis, characterization, crystal structure, molecular docking, and biological activities, J. Biochem. Mol. Toxicol. 38 (1) (2024) e23554.
[50] F.S. Tokalı, H. Şenol, Ş. Ateoglu, F. Akbaş, A series of quinazolin-4(3H)-one-morpholine hybrids as anti-lung-cancer agents: synthesis, molecular docking, molecular dynamics, ADME prediction and biological activity studies, Chem. Biol. Drug Des. 104 (1) (2024) e14599.
[51] M.A. Salem, S.Y. Abbas, M.H. Helal, A.Y. Alzahrani, Synthesis and antimicrobial evaluation of new 2-pyridinone and 2-iminochromene derivatives containing morpholine moiety, J. Heterocyclic Chem. 58 (11) (2021) 2117–2123.
[52] A. Kumari, R.K. Singh, Morpholine as ubiquitous pharmacophore in medicinal chemistry: deep insight into the structure-activity relationship (SAR), Bioorg. Chem. 96 (2020) 103578.
[53] F. Ahmadi Shourkaei, P. Rashidi Ranjbar, P. Taslimi, M. Mahdavi, Ugi four-multicomponent reaction based synthesis, in vitro, and in silico enzymatic evaluations of new pyrazino[1,2-a]indole-1,4-dione-indole-2-phenylacetamides as potent inhibitors against alpha-glucosidase and alpha-amylase, Chem. Biodivers. 21 (2) (2024) e202301292.
[54] E.E. Binici, H. Akincioglu, N. Kilinç, Indole-3-carbinol (I3C): inhibition effect on monoamine oxidase a (MAO-A), monoamine oxidase B (MAO-B) and cholinesterase enzymes, antioxidant capacity and molecular docking study, ChemistrySelect 8 (33) (2023) e202301727.
[55] D. Hu, N. Zhang, Y.Q. Zhang, C.M. Yuan, C.Y. Gong, Y.X. Zhou, W. Xue, Design, synthesis and biological activity of novel chalcone derivatives containing indole, Arab. J. Chem. 16 (6) (2023) 104776.
[56] Y. Chen, P. Yin, Q. Chen, Y. Zhang, Y. Tang, W. Jin, L. Yu, Neurodegenerative diseases and immune system: from pathogenic mechanism to therapy, Neural Regen. Res. (2025) 10.4103.

[57] B. Fu, W. Liu, Y. Wang, G. Li, Y. Wang, X. Huang, H. Shi, C. Qin, Design and synthesis of thiourea-conjugating organic arsenic D-glucose with anticancer activities, Molecules 29 (12) (2024) 2850.
[58] H. Şenol, Z. Çağman, T. Gencoglu Katmerlikaya, F. Sinan Tokali, New Anthranilic acid Hydrazones as Fenamate Isosteres: synthesis, characterization, molecular docking, dynamics & in silico ADME, in vitro anti-inflammatory and anticancer activity studies, Chem. Biodivers. 20 (8) (2023) e202300773.
[59] F.S. Tokalı, P. Taslimi, H. Usanmaz, M. Karaman, K. Sendil, Synthesis, characterization, biological activity and molecular docking studies of novel schiff bases derived from thiosemicarbazide: biochemical and computational approach, J. Mol. Struct. 1231 (2021).
[60] F.S. Tokalı, Synthesis and structural characterization of novel 2-Aminomethyl Quinazolin-4(3H)-ones as organic building blocks, Sakarya Univ. J. Sci. 26 (6) (2022) 1117–1130.
[61] E. Kalay, I.N. Korkmaz, F.N. Kacı, O.N. Aslan, P. Güller, F.S. Tokalı, R. Kalın, Design, synthesis, and biological studies of isoniazid-based hydrazone derivatives: antibacterial, anticancer, and enzyme inhibitory properties, Arch. Biochem. Biophys. 770 (2025) 110450.
[62] Y. Demir, F.S. Tokalı, E. Kalay, C. Türkeş, P. Tokalı, O.N. Aslan, K. Şendil, Ş. Beydemir, Synthesis and characterization of novel acyl hydrazones derived from vanillin as potential aldose reductase inhibitors, Mol. Divers. 27 (2022) 1713–1733.
[63] P.S. Patil, S.L. Kasare, N.B. Haval, V.M. Khedkar, P.P. Dixit, E.M. Rekha, D. Sriram, K.P. Haval, Novel isoniazid embedded triazole derivatives: synthesis, antitubercular and antimicrobial activity evaluation, Bioorg. Med. Chem. Lett. 30 (19) (2020) 127434.
[64] M.B. Muluk, P.S. Phatak, S.B. Pawar, S.T. Dhumal, N.N.M.A. Rehman, P.P. Dixit, P. B. Choudhari, K.P. Haval, Synthesis, antimicrobial, and antioxidant activities of new pyridyl- and thiazolyl-bearing carbohydrazides, J. Chin. Chem. Soc. 66 (11) (2019) 1507–1517.
[65] U. Ghaffar, Z. Batool, M. Tasleem, N. Sadeghian, P. Taslimi, S.N. Mali, K. A. Dahlous, R.D. Jawarkar, S.S. Gurav, X. Zhao, Synthesis, anti-Alzheimer evaluation and in silico study of (4-Methoxyphenyl) sulfonyl indole hybrid Thiosemicarbazones, Arch. Pharm. 358 (7) (2025) e70034.
[66] U. Farooq, M. Islam, Z. Batool, S.N. Mali, R.D. Jawarkar, S.S. Gurav, R.D. Alharthy, H. Şenol, N. Sadeghian, P. Taslimi, Design, synthesis, in vitro, and in silico studies of 5-(Diethylamino)-2-Formylphenyl Naphthalene-2-sulfonate based Thiosemicarbazones as potent anti-Alzheimer agents, Arch. Pharm. 358 (7) (2025) e70050.
[67] B. Zengin Kurt, D. Öztürk Civelek, E.B. Çakmak, Y. Kolcuoğlu, H. Şenol, B.N. Sağlık Özkan, A. Dag, K. Benkli, Synthesis of Sorafenib−ruthenium complexes, investigation of biological activities and applications in drug delivery systems as an anticancer agent, J. Med. Chem. 67 (6) (2024) 4463–4482.
[68] H. Şenol, G. Çelik Turgut, A. Şen, R. Sağlamtaş, S. Tuncay, İ. Gülçin, G. Topçu, Synthesis of nitrogen-containing oleanolic acid derivatives as carbonic anhydrase and acetylcholinesterase inhibitors, Med. Chem. Res. 32 (4) (2023) 694–704.
[69] F.S. Tokalı, H. Şenol, Ş. Ateşoğlu, P. Tokalı, F. Akbaş, Exploring highly selective polymethoxy fenamate isosteres as novel anti-prostate cancer agents: synthesis, biological activity, molecular docking, molecular dynamics, and ADME studies, J. Mol. Struct. 1319 (2025) 139519.
[70] F.S. Tokalı, H. Şenol, H.I. Yetke, E. Hacıosmanoğlu-Aldogan, Novel quinazoline-chromene hybrids as anticancer agents: synthesis, biological activity, molecular docking, dynamics and ADME studies, Arch. Pharm. 356 (11) (2023) e2300423.
[71] H. Şenol, K. Çokuludağ, A.S. Aktaş, S. Atasoy, A. Dağ, G. Topçu, Synthesis of new fatty acid derivatives of oleanane and ursane triterpenoids and investigation of their in vitro cytotoxic effects on 3T3 fibroblast and PC3 prostate cancer cell lines, Org. Commun. 13 (3) (2020) 114–126.
[72] A. Farzaliyeva, H. Şenol, P. Taslimi, F. Çakır, V. Farzaliyev, N. Sadeghian, I. Mamedov, A. Sujayev, A. Maharramov, S. Alwasel, İ. Gulçin, Synthesis and biological studies of acetophenone-based novel chalcone, semicarbazone, thiosemicarbazone and indolone derivatives: structure-activity relationship, molecular docking, molecular dynamics, and kinetic studies, J. Mol. Struct. 1321 (2025) 140197.
[73] I. Mamedov, H. Şenol, F. Naghiyev, V. Khrustalev, N. Sadeghian, P. Taslimi, New tetrahydro-isoquinoline derivatives as cholinesterase and α-glycosidase inhibitors: synthesis, characterization, molecular docking & dynamics, ADME prediction, in vitro cytotoxicity and enzyme inhibition studies, J. Mol. Liq. 404 (2024) 125006.